Plasma Spectral Diagnostic Analyses in Support of KALIF Experiments

J.J. MacFarlane and P. Wang

January 1994

UWFDM-943

FUSION TECHNOLOGY INSTITUTE

UNIVERSITY OF WISCONSIN

MADISON WISCONSIN

Plasma Spectral Diagnostic Analyses in Support of KALIF Experiments

J.J. MacFarlane and P. Wang

Fusion Technology Institute
University of Wisconsin
1500 Engineering Drive
Madison, WI 53706

http://fti.neep.wisc.edu

January 1994

UWFDM-943

Contents

1. Introduction

The purpose of this report is to provide a detailed description of work performed during the 1993 calendar year in the areas of spectral diagnostics, atomic physics, and radiation-hydrodynamics modeling for light ion beam-heated plasmas. This work has been supported by Kernforschungszentrum Karlsruhe (KfK) as part of a multiyear effort to develop and apply theoretical and computational models which can be used to study high energy density plasmas created by KALIF (the Karlsruhe Light Ion Facility). To date, we have developed and tested a series of collisional-radiative equilibrium (CRE) and atomic physics codes, and applied them to investigate the spectral properties of plasmas created by intense proton beams. In addition, we have coupled our non-LTE radiative transfer model into KATACO (the Karlsruhe target radiation-hydrodynamics code) in order to provide a more comprehensive treatment of line radiation transport effects in simulations of high energy density plasma experiments.

The tasks performed for our 1993 contract with KfK are listed in Table 1.1. The first task was to provide comprehensive users' guides for the CRE and atomic physics codes we have developed over the past several years. Included in this is a users' guide which details the coupling of the non-LTE radiative transfer (or CRE) modules with KATACO. The users' guides are provided in Section 4 of this report. (Note, however, in some versions of this report the users' guides have been provided separately in three-ring binders to provide a more convenient format for those actually using the codes.)

In the second task, we have investigated the extent to which lines of various atomic species are broadened and split by the Zeeman effect. The purpose of this study is to assess which lines offer the greatest potential for measuring the magnetic field strength in the diode plasma region during KALIF experiments. The results of this study are detailed in Section 3.

For the third task, spectral diagnostics calculations were performed to investigate the characteristics of K_α emission and absorption spectra for upcoming KALIF beam-plasma interaction experiments. Spectra were computed for thin fluorine (F) tracers, which are predicted to show good temperature-sensitivity for plasmas in the temperature range of 2 – 20 eV. Results of this study are detailed in Section 2.

The appendices of this report contain papers written by the authors during the past year which describe diagnostic analyses for intense light ion beam experiments. Although this work was supported by the Particle Beam Fusion Accelerator-II (PBFA-II)

Table 1.1. Tasks for 1993

1. Provide Users' Guides for standalone Collisional-Radiative Equilibrium (CRE) and Atomic Physics codes. Provide similar documentation for the KATACO-CRE interface. Update CRE interface with KATACO and documentation as necessary.

2. Examine Zeeman splitting of lines in KALIF diode plasma experiments to deduce B-field. Compute M-dependent oscillator strengths and Lande g factors for lines of interest.

3. Perform spectral diagnostics calculations in support of KALIF experiments. Perform CRE and atomic physics calculations to predict spectra for beam-plasma interaction experiments.

4. Document results in a final report to KfK.

program at Sandia National Laboratories, some of it should nevertheless be applicable to future KALIF experiments. Appendix A describes a portion of the work we have done to analyze Al K_α emission spectra measured in recent PBFA-II lithium beam experiments. Appendix B describes our modeling of multiple ionization processes which can occur as an ion beam interacts with a target. We expect to document additional parts of this work in the coming months, including work on using measured intensity ratios of K_α emission lines to diagnose plasma densities and temperatures, and the influence of dielectronic recombination on K_α emission spectra.

Finally, we wish to acknowledge valuable discussions with Drs. B. Goel, A. Ludmirsky, and H. Bluhm concerning upcoming beam-plasma interaction experiments on KALIF.

2. Diagnosing Conditions in Proton Beam-Heated Plasmas Using Fluorine K_α Emission and Absorption Spectroscopy

2.1. Introduction

K_α spectroscopy has been shown to be a valuable technique in determining plasma conditions in high temperature plasma experiments. K_α lines result from $2p \leftrightarrow 1s$ transitions. Thus, emission lines are produced by ions which have vacancies in the $1s$ shell and have at least one electron in the $2p$ shell. K_α absorption lines can be seen in the presence of an x-ray backlighter when ions have at least one vacancy in the $2p$ shell. Absorption spectroscopy of inner shell transitions has been used in laser-produced plasma experiments to diagnose pusher conditions in inertial confinement fusion (ICF) target implosions [1], to determine temperatures and densities in layered targets [2,3], and to measure opacities [4-6]. K_α emission lines have been observed in several types of experiments, including high-temperature tokamak plasmas [7], and beam-foil interactions [8,9]. K_α emission spectroscopy has also recently been shown to be an important diagnostic technique in plasmas created by intense light ion beams [10,11]. Measuring x-ray lines is a particularly valuable approach in such experiments because it allows one to probe the interior regions of targets by looking in a spectral region where opacity effects are reduced.

Bailey et al. [10] reported the first spectroscopic measurements of K_α x-ray satellites in an intense proton beam experiment. The emission spectra were obtained during Particle Beam Fusion Accelerator-II (PBFA-II) experiments at Sandia National Laboratories. K_α emission spectra have also recently been observed in intense Li-beam experiments on PBFA-II [12]. In these experiments, plasmas temperatures of 30 to 50 eV were achieved [11,13]. K_α emission lines are produced as the ion beam ejects K-shell electrons, which are subsequently filled by $2p$ electrons. Similarly, K_β lines are produced by $3p \rightarrow 1s$ transitions. The K_α lines from He-like to Ne-like ions exhibit small but detectable shifts to shorter wavelengths due to reduced screening effects in the partially filled L-shell. Thus, K_α satellite spectra provide a measure of the ionization distribution of the target plasma.

The purpose of this study is to show how K_α satellite spectroscopy can be used to diagnose conditions in plasmas at low-to-moderate temperatures ($2 \lesssim T \lesssim 20$ eV). This range of temperatures is expected to be achieved in initial intense proton beam-plasma interaction experiments performed on KALIF [14]. In initial KALIF experiments, a B_θ

diode will be used to focus the proton beam to achieve a $1-2$ MeV power density of about 0.2 TW/cm^2. In later experiments, an applied-B diode will be used to achieve higher beam power densities and higher plasma temperatures. To diagnose plasma temperatures in the 2 to 20 eV range, it is proposed that a thin fluorine tracer be used as the primary diagnostic in the target. The use of fluorine offers several advantages. First, in its neutral state is has a partially filled L-shell. Therefore, the K_α satellites are noticeably blue-shifted even for the lower ionization stages. Second, the F K_α satellites reside at a wavelength that can be readily observed ($\lambda = 17.0 - 18.5$ Å). At longer wavelengths, which occur for lower-Z materials, it becomes more difficult to obtain good spectral measurements. Third, thin F tracer layers can be easily manufactured [15]. In addition, tracers made of NaF or MgF compounds can provide additional constraints for diagnosing plasma conditions because the Na and Mg K_α lines can potentially be observed simultaneously with the F lines. In this section, however, we focus our attention only to the F K_α satellites because they provide the best diagnostic information at low temperatures.

In Section 2.2 we describe the CRE and atomic physics models used to compute the K_α and K_β satellite spectra. Results are presented in Section 2.3, where we discuss the sensitivity of both absorption and emission spectra to tracer temperature, density, and thickness. We also discuss opacity effects of the tamper regions and tracer layer, and the sensitivity of spectra to the crystal spectral resolution. A summary of this investigation is presented in Section 2.4.

2.2. Theoretical Models

Atomic level populations are computed by solving multilevel statistical equations self-consistently with the radiation field and ion beam properties. Processes considered in the statistical equilibrium equations are: collisional (electron impact) excitation, deexcitation, ionization, and recombination; photoexcitation, spontaneous and stimulated emission; photoionization, radiative and dielectronic recombination; and ion beam-impact ionization of K-shell electrons, and Auger ionization. Collisional coupling between states is "complete" in the sense that for each ion all non-autoionizing states are collisionally coupled together, as are all autoionizing levels. Coupling between non-autoionizing and autoionizing levels takes place via ion-impact ionization, Auger ionization, and spontaneous decay. Radiative coupling between levels is modeled for all transitions with oscillator strengths greater than 10^{-5}. This level of detail allows one to

accurately track transitions into, out of, and between autoionizing levels, which becomes necessary when using the intensity ratios of individual lines as temperature and density diagnostics.

In our calculations, we consider a total of 640 atomic energy levels distributed over all 10 ionization stages of fluorine. Roughly, 50% of these were autoionizing levels, of which 270 have M-shell spectators. Thus, K_α lines with M-shell spectator electrons and K_β lines were considered. Energy levels and oscillator strengths were calculated using a configuration interaction (CI) model with Hartree-Fock wavefunctions. The line spectrum is treated with full intermediate coupling. Electron-impact collision data were computed using a combination of distorted wave, Coulomb-Born, and semi-classical impact parameter models. For forbidden transitions, distorted wave calculations were performed.

Radiation transfer effects were calculated using an escape probability model [16,17]. Radiative processes do not significantly affect the populations of the non-autoionizing states at relatively high densities and low temperatures ($n \gtrsim 10^{20}\,\mathrm{cm}^{-3}$, $T \lesssim 10$ eV) because the plasma tends to be collisionally dominated and the plasma populations are close to LTE. Opacity due to resonant self-absorption, however, can significantly impact the spectrum. Bound-bound, bound-free (including inner-shell), and free-free transitions are considered in the spectral calculations. Voigt profiles are assumed for the lines. Line widths include contributions from natural, Auger, Doppler, and Stark broadening.

Autoionizing levels are populated as the beam ejects K-shell electrons. The proton impact ionization rate is:

$$R_{ii^*} = n_i \, \sigma_K(E_B) \, J_B \, ,$$

where J_B and E_B are the current density (particle flux) and energy per particle of the beam, σ_K is the cross section, and n_i is the number density of particles in level i. The indices i^* and i refer the autoionizing state and the initial state (prior to K-shell ejection), respectively. In the CRE calculations, the beam is assumed to be monoenergetic and spatially uniform. It is worth noting that the plasma is heated primarily by the interaction of the beam with outer (L-shell) electrons. The ejection of the K-shell electrons serves mainly as a diagnostic.

Proton impact ionization cross sections for ground and excited states of F I, F IV, and F VII are shown in Fig. 2.1 as a function of the proton beam energy. These

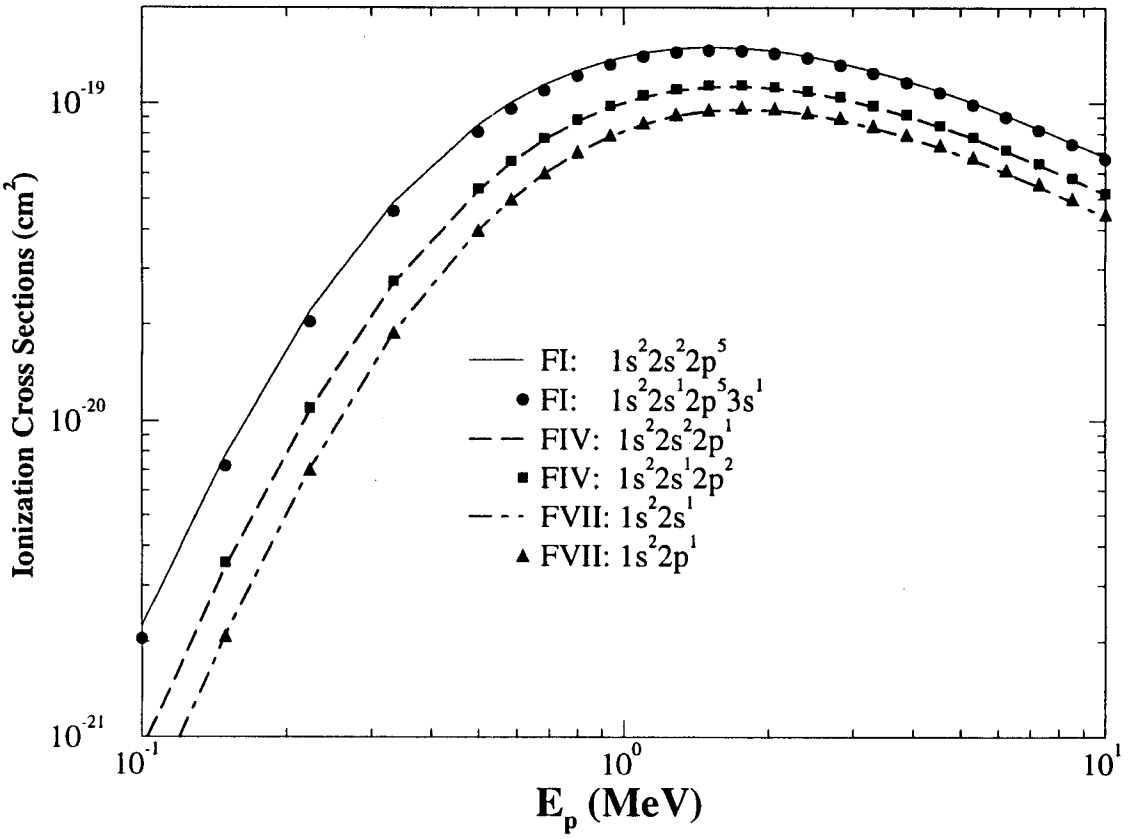

Figure 2.1. Dependence of proton impact ionization cross section on proton beam energy for ground and excited states of F I, F IV, and F VII.

cross sections were computed using a CPSSR model (Coulomb-deflection, perturbed-stationary-state, and relativistic wave function) [see Appendix B], which has been shown to more accurately predict cross sections at relatively low ion projectile energies than a plane-wave Born approximation model without correction terms [18]. The excited state cross sections (filled symbols) are for excited state configurations of the type $1s^2\,2s^1\,2p^5\,3s^1$, $1s^2\,2s^1\,2p^2$, and $1s^2\,2p^1$ for F-like, B-like, and Li-like fluorine, respectively. The cross section represents the sum over all levels within the initial and final configurations. It is seen that the cross sections decrease with increasing ionization state, with the Li-like cross section being approximately 40% lower than that of neutral fluorine. Relatively little change is seen between the cross sections of ground state and low-lying excited state configurations. Note also that there is relatively little change in the cross section between 1 and 3 MeV. Thus, uncertainties associated with the proton beam not being monoenergetic should be minimal in this range.

In addition to proton impact ionization, emission line intensities are dependent on the fluorescence yields. Fluorescence yields and Auger rates were calculated for each autoionizing level using an L-S coupling formalism with Hartree-Fock wavefunctions. The fluorescence rate (i.e., the rate at which K_α photons are emitted) from level i^* to level j is given by

$$R_{i^*j} = n_{i^*}\, A_{i^*j}\,,$$

where A_{i^*j} is the spontaneous decay rate. The Auger rate can be expressed as

$$R_{i^*\kappa} = n_{i^*}\,[Y_{i^*}^{-1} - 1] \sum_j A_{i^*j}\,,$$

where Y_{i^*} is the fluorescence yield of the autoionizing level i^*, and the index κ refers to the ground state of the next higher ionization stage.

Fluorescence yields for each autoionizing level are plotted in Fig. 2.2 (small filled circles) as a function of the wavelength at which K_α lines are emitted. Also shown are configuration-averaged fluorescence yields (open squares) and those averaged over levels in the ground state configuration of each ion (gray circles). Note the wide spread in fluorescence yield throughout the spectral region of the K_α satellites. Clearly, developing a good understanding of the structure within the major satellite features (i.e., for each ionization state) and the dependence of intensity ratios of individual K_α lines requires that atomic level-dependent fluorescence yields be included in the analyses of K_α emission spectra. Also note that the fluorescence yields increase substantially for ionization stages higher than Be-like fluorine. For He-like fluorine, the yield is of course unity as $1s^1\,2p^1$

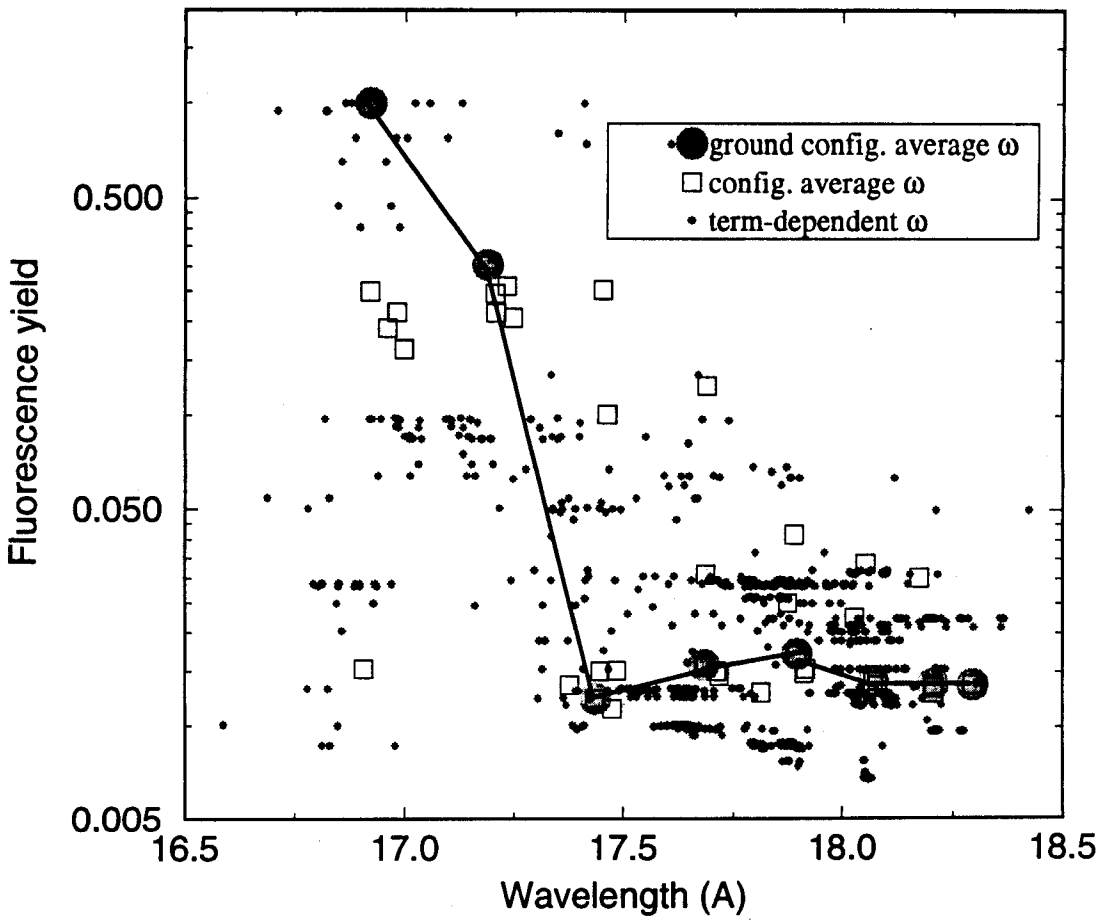

Figure 2.2. Fluorescence yields for fluorine autoionizing levels as a function of wavelength of their K_α transitions.

levels are non-autoionizing. Because of the higher fluorescence yields, the intensities of the Li-like and He-like lines can be significantly stronger than the K_α satellites of lower ionization stages, which typically have fluorescence yields $\sim 10^{-2}$.

2.3. Results

Calculations have been performed for a planar "plastic sandwich" target of the type illustrated in Fig. 2.3. The total thickness of the target is about 2 – 5 μm, which is small compared to the stopping range of 1 MeV protons in plastic. The target consists of a thin tracer layer of NaF ($L \sim 0.1 - 1\,\mu$m) sandwiched between 2 plastic tampers with a thickness of 1 – 2 μm each. The purpose of the tampers is to keep to density in the tracer region approximately uniform as the target is heated and expands. The tampers are limited to this thickness so that the attenuation of tracer K_α photons by the tamper is not excessive.

The tracer thickness is dictated by several considerations. For experiments involving absorption spectroscopy, tracer thicknesses of 500 – 2000 Å are optimum [4,5]. This is because the optical depths of the K_α lines are $\sim 10^0 - 10^1$ at this thickness. For tracer thicknesses much greater than this the lines become saturated. In the case of emission spectroscopy, one would like the tracer to be as thin as possible to mitigate the effects of opacity on the observed spectra, but still be thick enough to have enough signal (photons) to detect. The minimum thickness depends on: (1) the material properties of the tracer and the ability to manufacture it, (2) the sensitivity of the detector in the tracer's K_α spectral region, and (3) the strengths of any external radiation sources (e.g., Bremsstrahlung from the diode region). In recent Li-beam experiments on PBFA-II 2000 Å-thick Al tracers were found to produce a sufficient number of K_α photons for measuring the x-ray spectra at high resolution ($\lambda/\Delta\lambda \simeq 1200$) [12].

2.3.1. Tracer and Tamper Thicknesses

The dependence of the flux emitted in the fluorine K_α spectral region on tracer thickness is shown in Fig. 2.4. This represents the calculated intensity between 0.4 – 1.1 keV along a line of sight normal to the planar target. The calculations were performed for a tracer temperature of $T = 10$ eV and ion density of $n = 6 \times 10^{20}\,\mathrm{cm}^{-3}$. This density corresponds roughly to that expected at the time of peak temperature. This is assumed to be $\approx 10^{-2}\, n_o$ ($n_o \equiv$ solid density). The plasma thickness in each calculation was

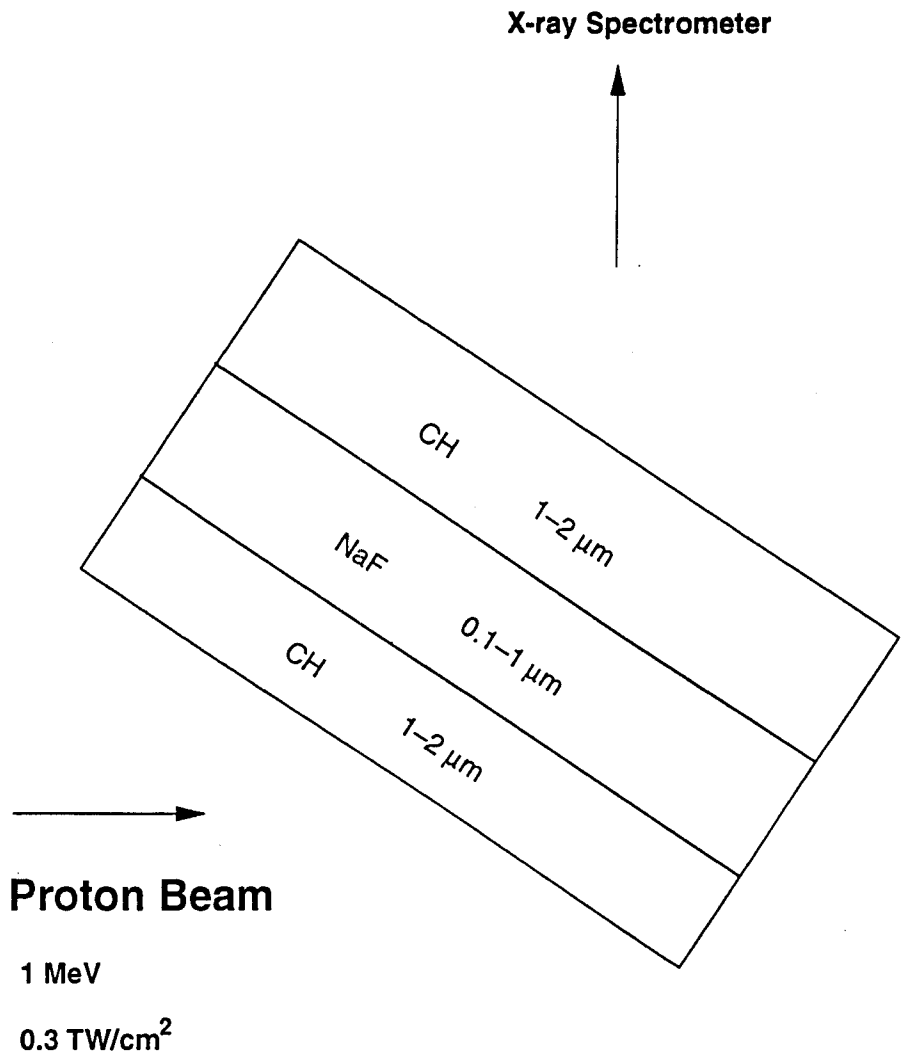

Figure 2.3. Schematic illustration of "plastic sandwich" target with NaF tracer.

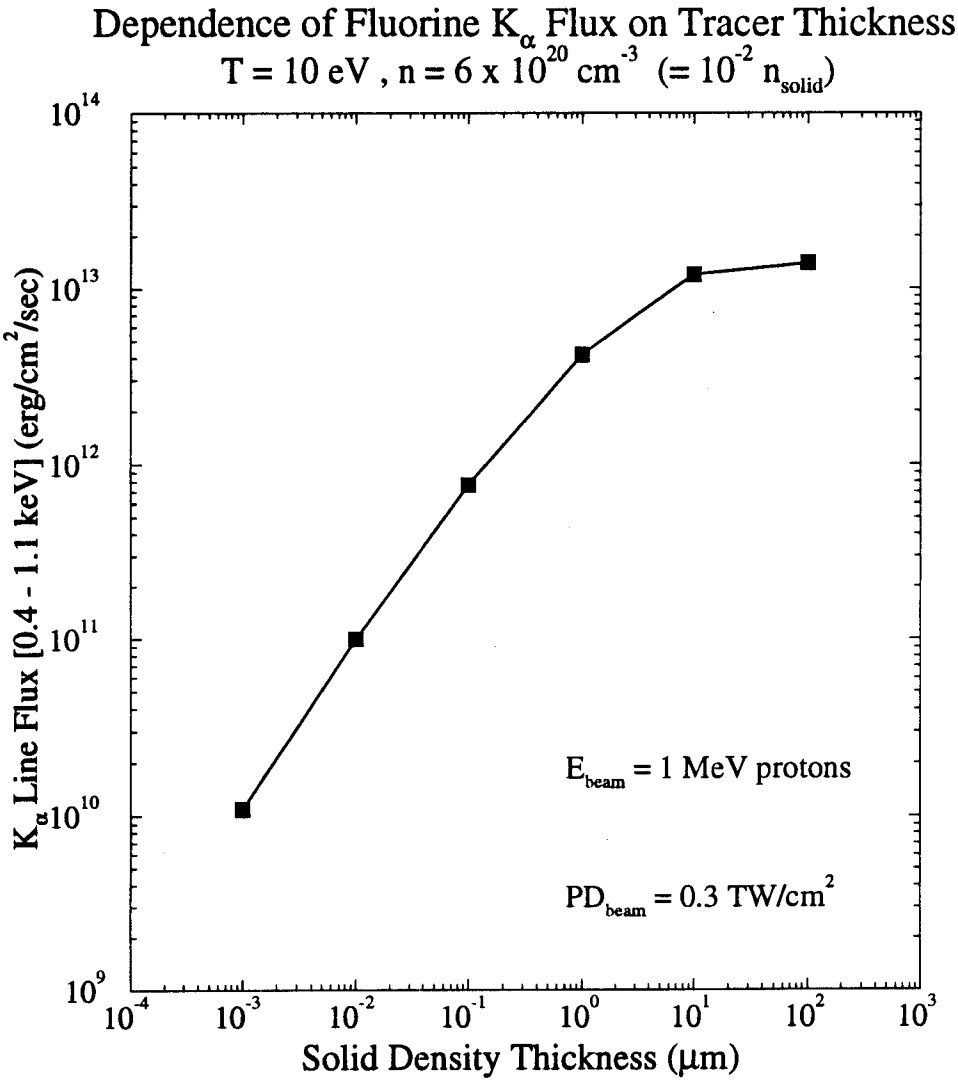

Figure 2.4. Dependence of total K_α flux (integrated over frequency band from 0.4 to 1.1 keV) on thickness of tracer layer.

therefore 100 times the solid density thickness shown in Fig. 2.4. In each case, the beam was assumed to be 1 MeV protons with a power density of 0.3 TW/cm^2.

For thin tracers ($L_o < 10^{-1}\,\mu$m; $L_o \equiv$ solid density thickness) the emitted flux is nearly proportional to the tracer thickness because the plasma is optically thin. For $L_o \gtrsim 10^{-1}\,\mu$m, the K_α lines become optically thick and the flux is seen to increase slower than linearly. When the tracer thickness is $\gtrsim 10\,\mu$m the flux becomes constant. This occurs because the plasma becomes optically thick at all frequencies in this spectral region. Therefore, increasing the tracer thickness beyond 10 μm will not significantly increase the number of K_α photons reaching the detector. Instead, the effect is to skew the satellite spectrum toward apparent higher ionization stage [11], making it more difficult to determine plasma conditions from emission spectra. Thus, the optimum tracer thickness for experiments utilizing emission spectroscopy is $\sim 0.1-1\,\mu$m. When absorption spectral measurements are made, the tracer thickness should be at the lower end of this range.

The attenuation of tracer K_α photons by the tamper can potentially be severe and must be considered in the target design. This is true both for photons emitted by the tracer layer and for the absorption of x-ray backlighter photons in an absorption experiment. The carbon K-shell photoionization cross section at 18 Å is about 0.12 Mbarns. Assuming a density of 4×10^{22} C atoms/cm^3 in the plastic tampers, the absorption coefficient is 0.5 μm^{-1} at 18 Å. Thus, photons at this wavelength will be attenuated about 40% ($\exp(-\kappa L)$) for each micron of plastic. Greater attenuation occurs along lines-of-sight not perpendicular to the target surface. Thus, the tamper thickness must be kept to about 1 – 2 μm or less.

It is worth noting that Al, a material commonly used in high energy density plasma experiments because of its low expense and ease in fabrication, may also be a suitable tamper when using F, Na, or Mg as tracers. Since the Al K-shell photoabsorption edge lies shortward of the K_α satellites of these tracers, attenuation arises only from the Al L-shell. At 18 Å, the Al L-shell cross section is 0.15 Mb, which is only about 25% higher than the K-shell cross section of plastic tampers at this wavelength.

2.3.2. Dependence of K_α Satellite Spectra on Temperature and Density

To assess the sensitivity of F K_α emission and absorption spectra to target plasma conditions, we performed a series of CRE calculations for temperatures from 2 to 20 eV. The ion densities ranged from 10^{19} cm^{-3} to 10^{22} cm^{-3}, which are typical of those occurring

in intense light ion beam experiments during the time the beam irradiates the target. In each calculation the target is irradiated with a 1 MeV proton beam with a power density of 0.3 TW/cm^2. The original (pre-expansion) NaF thickness was $L_o = 2000$ Å in each case, assuming a solid density thickness for fluorine of $n_o(F) = 3.67 \times 10^{22}$ atoms/cm^3. The plasma (post-expansion) thickness was simply $L = L_o(n/n_o)$.

Results for emission and absorption spectra are shown in Figs. 2.5 and 2.6 (additional spectra are reported in [19]). The temperature dependence for plasmas at $n = 10^{20}\,\mathrm{cm}^{-3}$ is shown in Fig. 2.5, while the density dependence for plasmas at $T = 10$ eV is shown in Fig. 2.6. In each case, the emission spectrum is plotted on the left, while the absorption spectrum (transmission = $\exp(-\tau)$, where τ = optical depth) is plotted on the right. The wavelength regions of the K_α lines of various fluorine ions are identified in the emission spectra, while the K_β lines are identified in the absorption spectra. Note the absorption spectra are plotted over a larger wavelength range. This is because K_β transitions are readily seen in absorption, while they are rather weak in emission. At $T = 2$ eV, both K_α and K_β lines are seen in absorption for neutral and O-like fluorine. N- and O-like K_α are the dominant emission lines. Neutral fluorine is not seen in emission because the autoionization states are populated by proton impact ionization processes (i.e., the O-like emission lines originate from neutral fluorine). K_β emission line intensities are about 3 orders of magnitude lower. This is simply due to the fact that the K_β transitions originate from configurations of the type $1s^2\,2s^m\,2p^n\,3l\,(l = s, p, d)$, which are less populated than the lower lying energy levels. K_β lines can of course be seen in absorption because the opacity depends on the *lower* state of the transition ($1s^1\,2s^m\,2p^n\,3p^1 \overset{K_\beta}{\longleftrightarrow} 1s^2\,2s^m\,2p^n$).

As the target is heated to 5 eV, both K_α and K_β lines are seen for N-like F in absorption, while C-, B-, and N-like K_α satellites are seen in emission. At this temperature, N- and O-like F are the dominant ionization stages, as is reflected in the absorption spectrum. Higher ionization stages appear in emission compared to absorption for two reasons: (1) the K_α emission lines are produced from low lying states of the next lower ionization stage via proton impact ionization, and (2) there is a slight skewing of the spectrum toward apparent higher ionization stage due to resonant self-absorption. For these conditions, the N- and O-like intensities are reduced by opacity effects while C- and B-like K_α lines are unaffected.

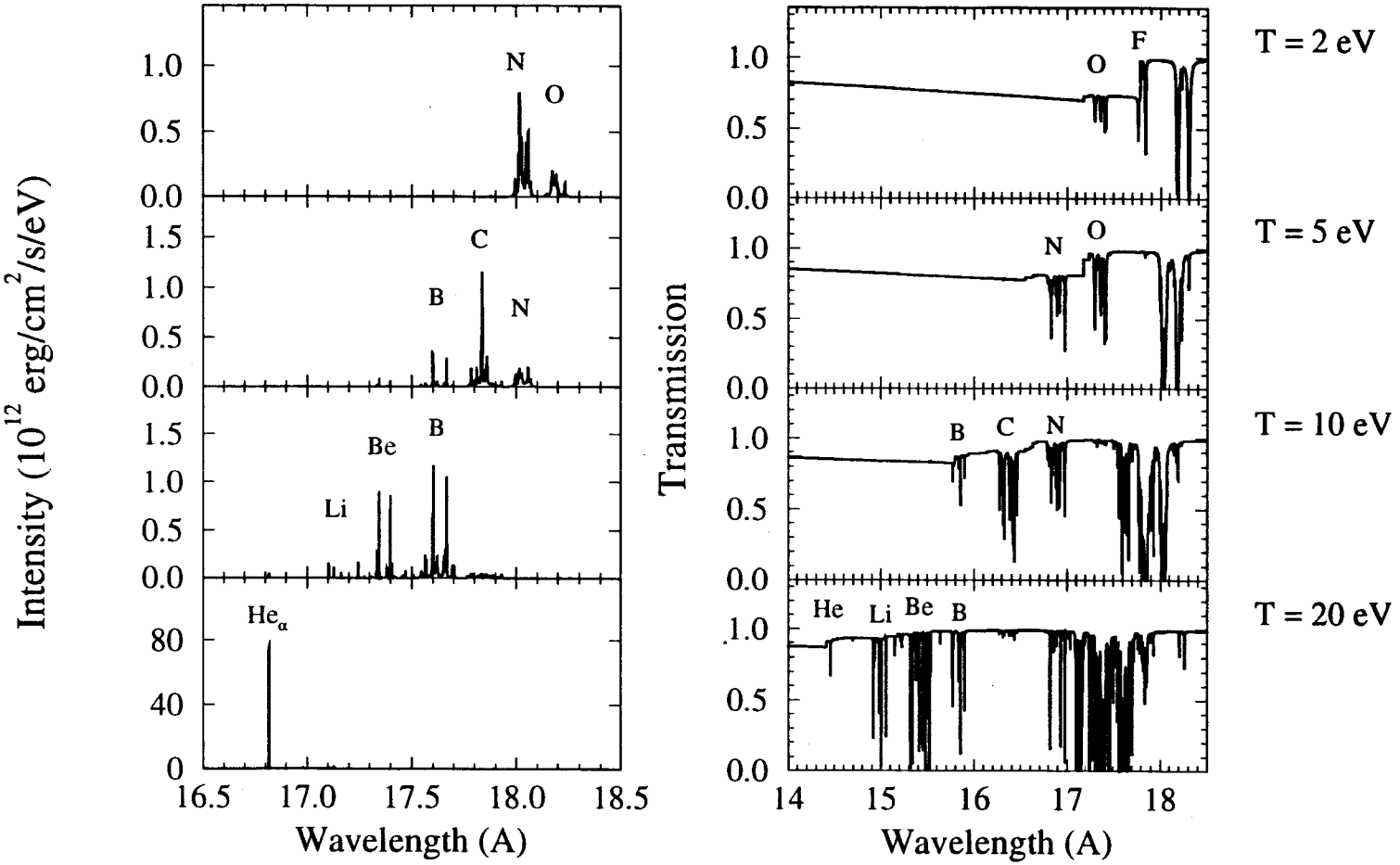

Figure 2.5. Temperature dependence of fluorine K_α emission (left) and absorption (right) spectra. In each case, $n = 10^{20}$ ions/cm^3 and the original thickness of the tracer layer was 2000 Å.

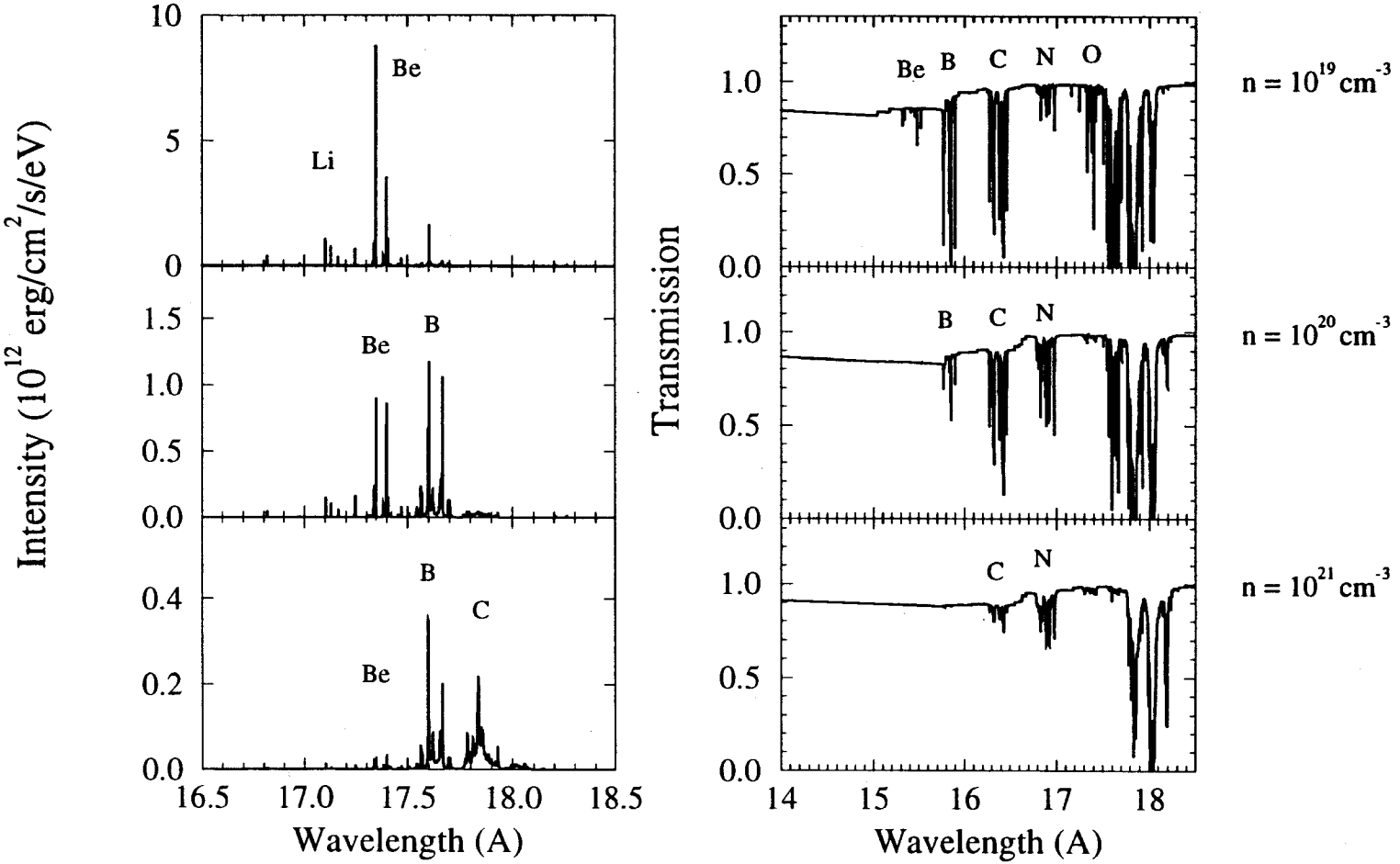

Figure 2.6. Density dependence of fluorine K_α emission and absorption spectra. In each case, $T = 10$ eV and the original thickness of the tracer layer was 2000 Å.

At $T = 10$ eV, K_α and K_β satellites from B-, C-, and N-like fluorine are seen in absorption, while the Li-like through B-like satellites are strongest in emission. Note that the strongest He-like resonance line (He_α : $1s^1\,2s^{1\,1}P \rightarrow 1s^{2\,1}S$ at $\lambda = 16.8$ Å) begins to appear at this temperature. Since the upper state of this transition is not an autoionizing level, it has a fluorescence yield of unity. By comparison, the fluorescence yields for the K_α satellites of lower ionization stages is roughly 1%. Because of this the He_α line can be significantly stronger than the K_α lines from lower ionization stages. This is seen in the $T = 20$ eV emission spectrum. Note the change in the intensity scale for this temperature. Also, the Li-like K_α lines are stronger than the K_α satellites at lower temperature. This also is due to its higher fluorescence yield (see Fig. 2.2).

Figure 2.6 shows the density dependence of F K-shell emission and absorption spectra at $T = 10$ eV. The densities shown ($n = 10^{19} - 10^{21}\,\mathrm{cm}^{-3}$) span the range where the target plasma temperatures are expected to be highest. The results show the trend to lower ionization stages as the density increases. For instance, the absorption spectra show that B- and C-like fluorine are the dominant ionization stages at 10^{19} cm^{-3}, while N-like F is the dominant stage at 10^{21} cm^{-3}. Similarly, the peak emission moves from Be-like F at 10^{19} cm^{-3} down to B- and C-like at 10^{21} cm^{-3}.

2.3.3. Dependence on Spectral Resolution

If individual or small groups of K_α lines can be spectrally resolved, one can use K_α line intensity ratios to diagnose plasma conditions. This is illustrated in Fig. 2.7, where the emission spectrum for a $T = 10$ eV, $n = 10^{20}$ cm^{-3}, 37 μm-thick ($L_o = 1000$ Å) plasma is plotted assuming 3 different x-ray crystal spectral resolutions. Note that as the resolution increases from 500 to 2000 significantly more structure can be seen for each ionization stage. For instance, at $\lambda/\Delta\lambda = 500$ (thin solid curve), the Li-like qr and bda lines near 17.1 Å (see Table 2.1 for line identifications) are blended together, whereas at a resolution of 2000 (dashed curve) they are clearly distinguished. Similarly, 6 features from B-like fluorine are resolved for the $\lambda/\Delta\lambda = 2000$ case, while they are blended into 2 features when the resolution is only 500.

It is important to note that the intrinsic line widths are small compared to the spectral resolution for the plasma conditions. Because of this, considerably more spectral information — and with that constraints on plasma conditions — can be obtained by using higher resolution crystals in beam-plasma interaction experiments. The intrinsic

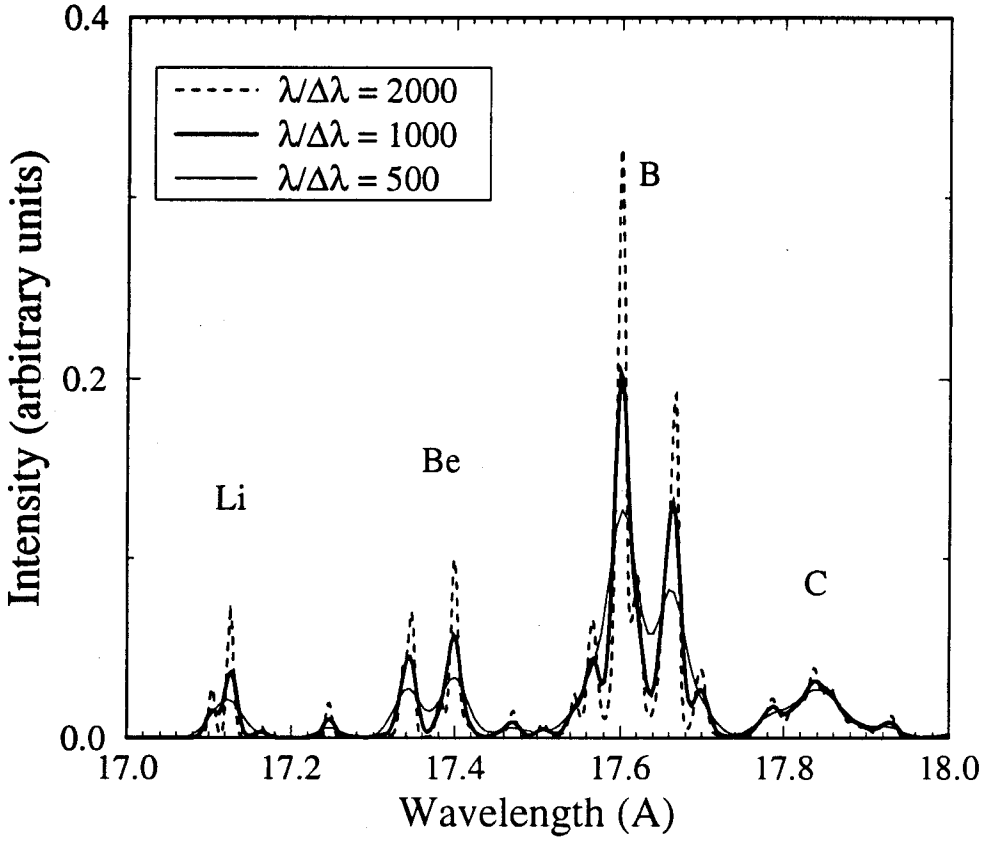

Figure 2.7. Dependence of K_α emission spectrum on X-ray crystal spectral resolution. In each calculation, $T = 10$ eV, $n = 10^{20}$ ions/cm^3, and $L_o = 1000$ Å.

line widths tend to be dominated by the Auger decay rate. With the exception of K_β lines (which can be seen in absorption) and K_α lines with M-shell spectator electrons (which are predicted to be very weak in emission), Stark broadening is relatively unimportant (see also Section 4 of [11]). If the widths of K_β lines can be measured in absorption, this may provide an additional density constraint for the target plasma.

2.3.4. Plasma Diagnostics Using Measured K_α Line Intensity Ratios

In this section we present the results of preliminary calculations for determining plasma conditions using the relative strengths of K_α emission lines. A series of CRE calculations was performed for optically thin plasmas of uniform temperature and density, irradiated with a 1 MeV, 0.3 TW/cm^2 proton beam. (Opacity effects due to the finite thickness of the target will be studied in future calculations.) Calculations were performed of a grid of temperatures and ion densities given by:

$$5 < T < 25 \text{ eV}$$
$$10^{18} < n < 10^{21} \text{ cm}^{-3} .$$

Line intensities were computed at each T, n grid point. Results for several combinations of He-, Li-, and Be-like fluorine line intensity ratios are shown in Fig. 2.8. The line identifications are given in Table 2.1. We focus on K_α lines from relatively high ionization stages because there is less blending of lines because of the simpler atomic structure of these ions; i.e., there are fewer lines per ion. Based on our previous comparisons with experimental data for Al, it is expected that the calculated wavelengths are accurate to better than 0.01 Å (see Appendix A). Two plots are shown for each line combination: on the top, intensity ratios are plotted as a function of temperature with the density held constant, while the reverse is true for the bottom plot.

Figures 2.8(a) through 2.8(c) show 3 examples of temperature-sensitive ratios. Note that in each case the lines used are from adjacent ions. Recall that a good temperature indicator is one where the relative intensities have only a weak dependence on the density, but strong dependence on the temperature. The best temperature indicator appears to be the ratio of the He_α line ($\lambda = 16.82$ Å) to the Li-like st line ($\lambda = 16.98$ Å). For instance if the lines were observed to have equal strength (i.e., a ratio = 1), the predicted temperature would be about 7 eV throughout the entire density range of $10^{18} - 10^{21}$ cm^{-3}.

Table 2.1. Prominent Fluorine K_α Lines

	Lower State	Upper State	Comment	λ(Å)
He-like	$1s^2\ ^1S$	$1s^1 2p^1\ ^1P$	He_α	16.818
	$1s^2\ ^1S$	$1s^1 2p^1\ ^3P$	He-IC	16.952
Li-like	$1s^2 2p^1\ ^2P$	$1s^1 2p^2\ ^2S$	mn	16.936
	$1s^2 2s^1\ ^2S$	$2s^1 2p^1(^1P) 1s^1\ ^2P$	st	16.978
	$1s^2 2s^1\ ^2S$	$2s^1 2p^1(^3P) 1s^1\ ^2P$	qr	17.104
	$1s^2 2p^1\ ^2P$	$1s^1 2p^2\ ^2P$	bda	17.126
	$1s^2 2p^1\ ^2P$	$1s^1 2p^2\ ^2D$	kj	17.157
Be-like	$1s^2 2s^1 2p^1\ ^3P$	$1s^1 2s^1 2p^2\ ^3P$ (2)	λ_6	17.164
	$1s^2 2s^1 2p^1\ ^3P$	$1s^1 2s^1 2p^2\ ^3S$	λ_7	17.246
	$1s^2 2p^2\ ^1D$	$1s^1 2p^3\ ^1P$	λ_8	17.274
	$1s^2 2p^2\ ^3P$	$1s^1 2p^3\ ^3P$	λ_1	17.314
	$1s^2 2s^1 2p^1\ ^1P$	$1s^1 2s^1 2p^2\ ^1S$	λ_2	17.332
	$1s^2 2s^2\ ^1S$	$1s^1 2s^2 2p^1\ ^1P$	λ_2	17.337
	$1s^2 2s^1 2p^1\ ^1P$	$1s^1 2s^1 2p^2\ ^1P$	λ_2	17.346
	$1s^2 2s^1 2p^1\ ^3P$	$1s^1 2s^1 2p^2\ ^3D$	λ_3	17.382
	$1s^2 2s^1 2p^1\ ^3P$	$1s^1 2s^1 2p^2\ ^3P$	λ_4	17.398
	$1s^2 2p^2\ ^3P$	$1s^1 2p^3\ ^3S$	λ_4	17.407
	$1s^2 2p^2\ ^1D$	$1s^1 2p^3\ ^1D$	λ_4	17.414
	$1s^2 2p^2\ ^3P$	$1s^1 2p^3\ ^3D$	λ_5	17.454
	$1s^2 2p^2\ ^1S$	$1s^1 2p^3\ ^1P$	λ_5	17.465
	$1s^2 2s^1 2p^1\ ^1P$	$1s^1 2s^1 2p^2\ ^1D$	λ_5	17.471

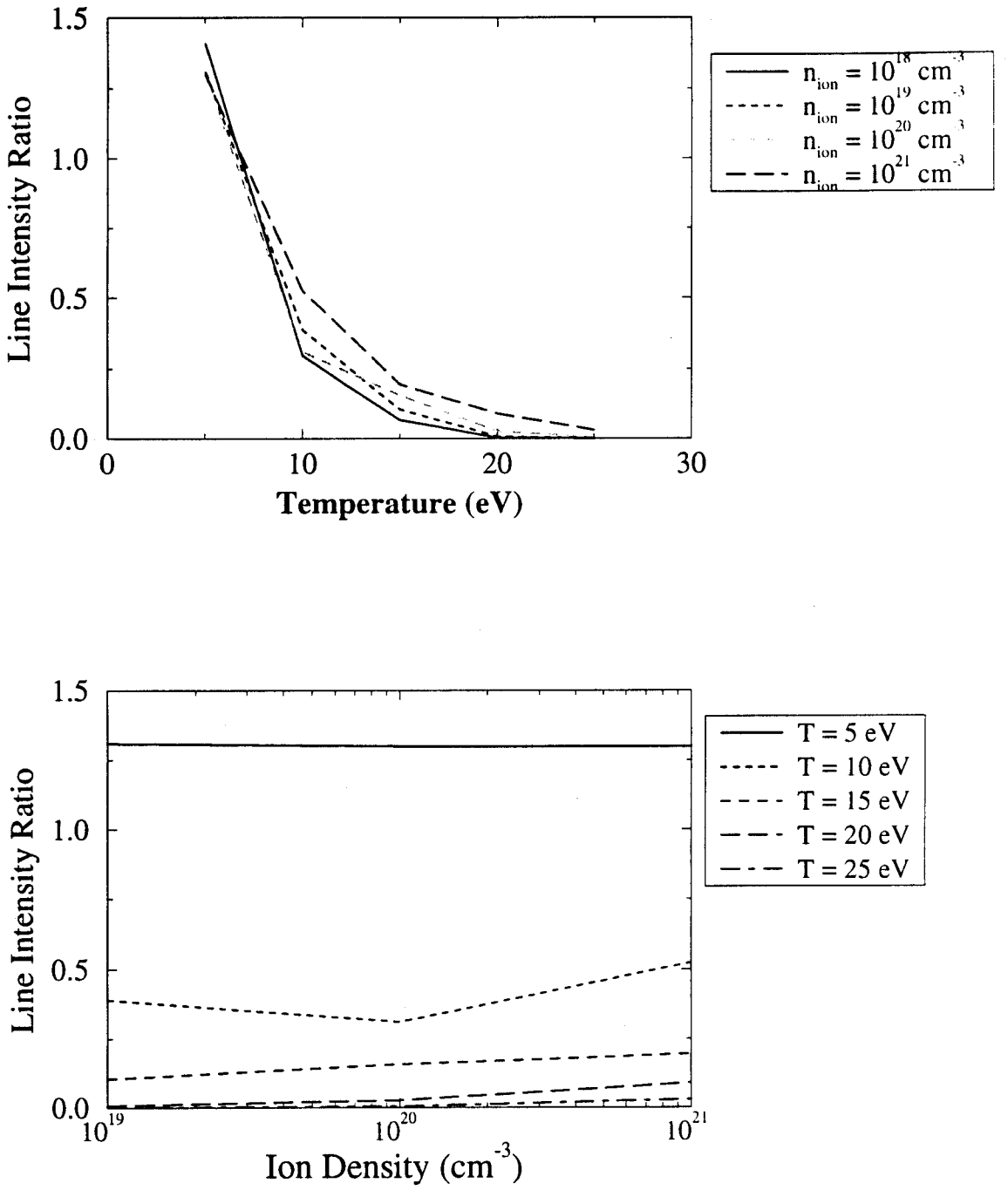

Figure 2.8(a). Temperature and density dependence of He_α/Li(st) intensity ratio.

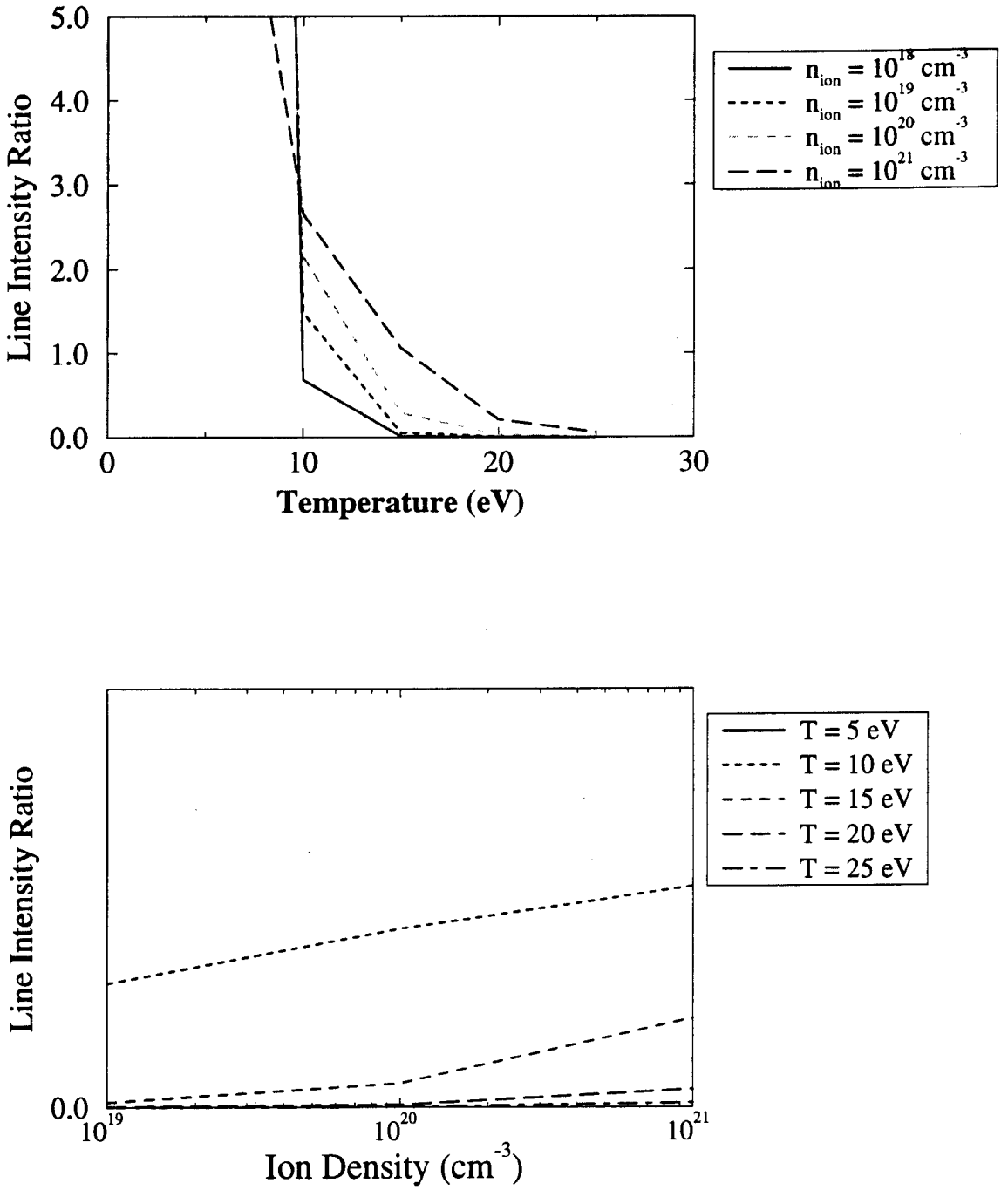

Figure 2.8(b). Temperature and density dependence of Be(λ_7)/Li(bda) intensity ratio.

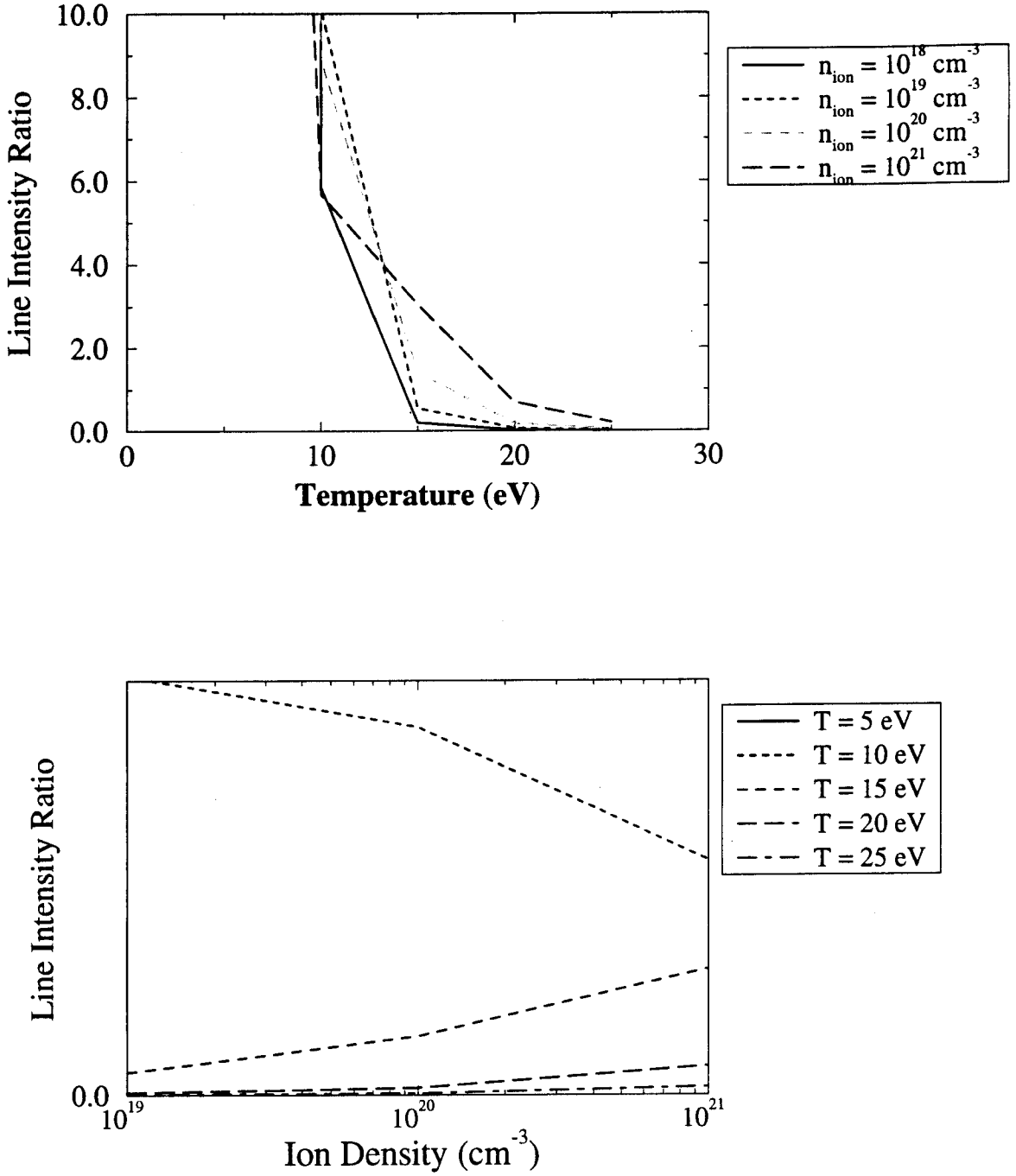

Figure 2.8(c). Temperature and density dependence of Be(λ_2)/Li(qr) intensity ratio.

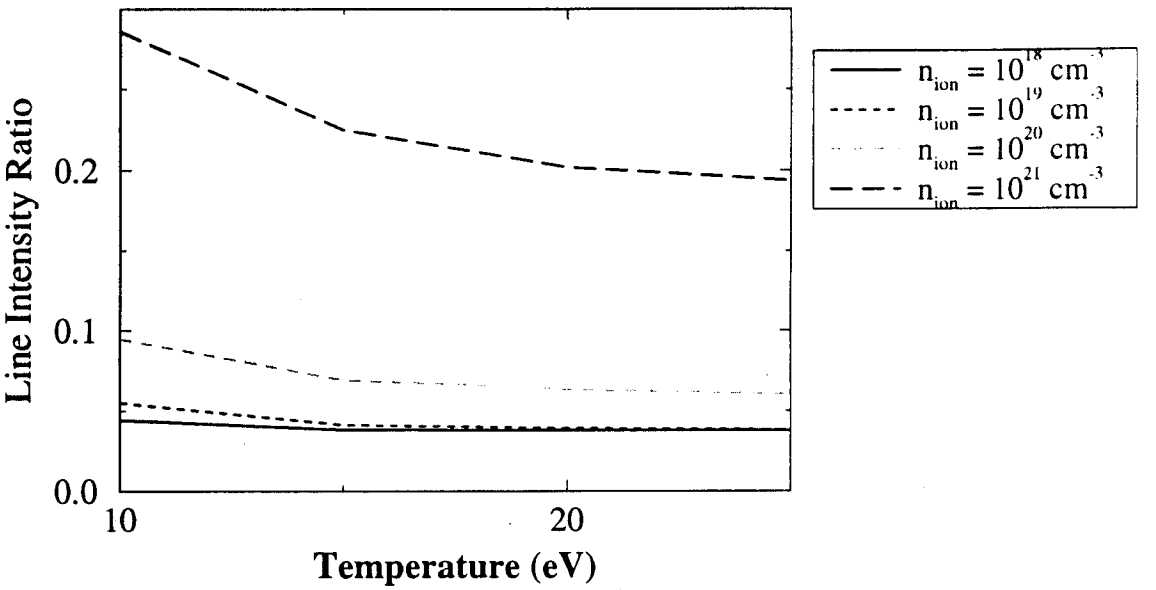

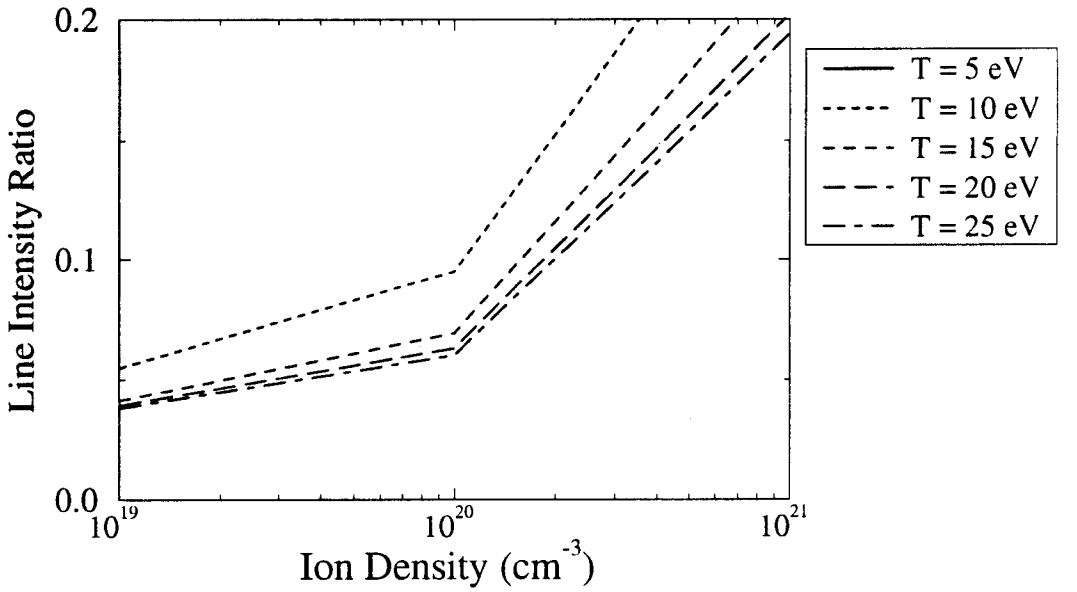

Figure 2.8(d). Temperature and density dependence of Li(kj)/Li(bda) intensity ratio.

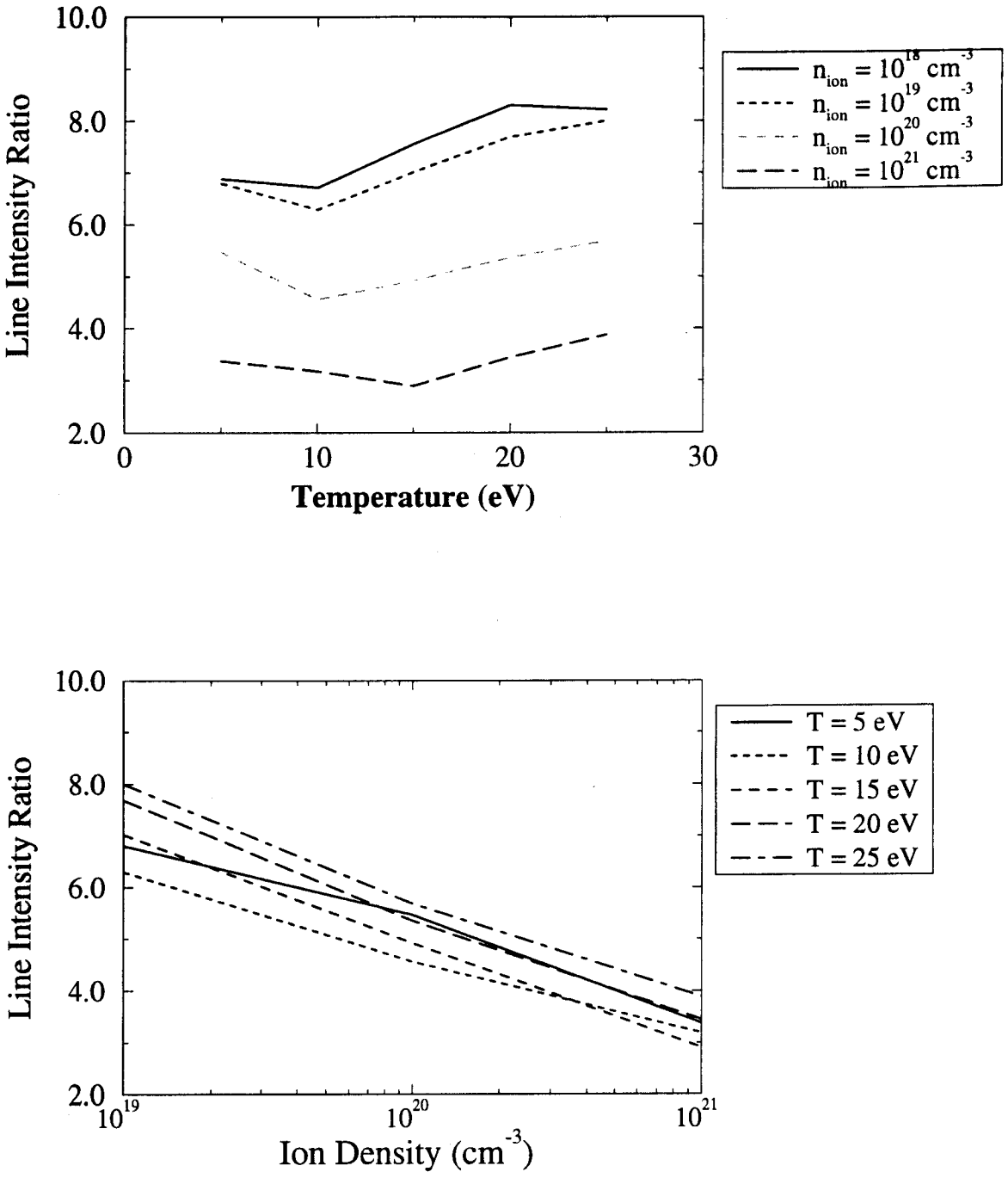

Figure 2.8(e). Temperature and density dependence of Be(λ_4)/Be(λ_3) intensity ratio.

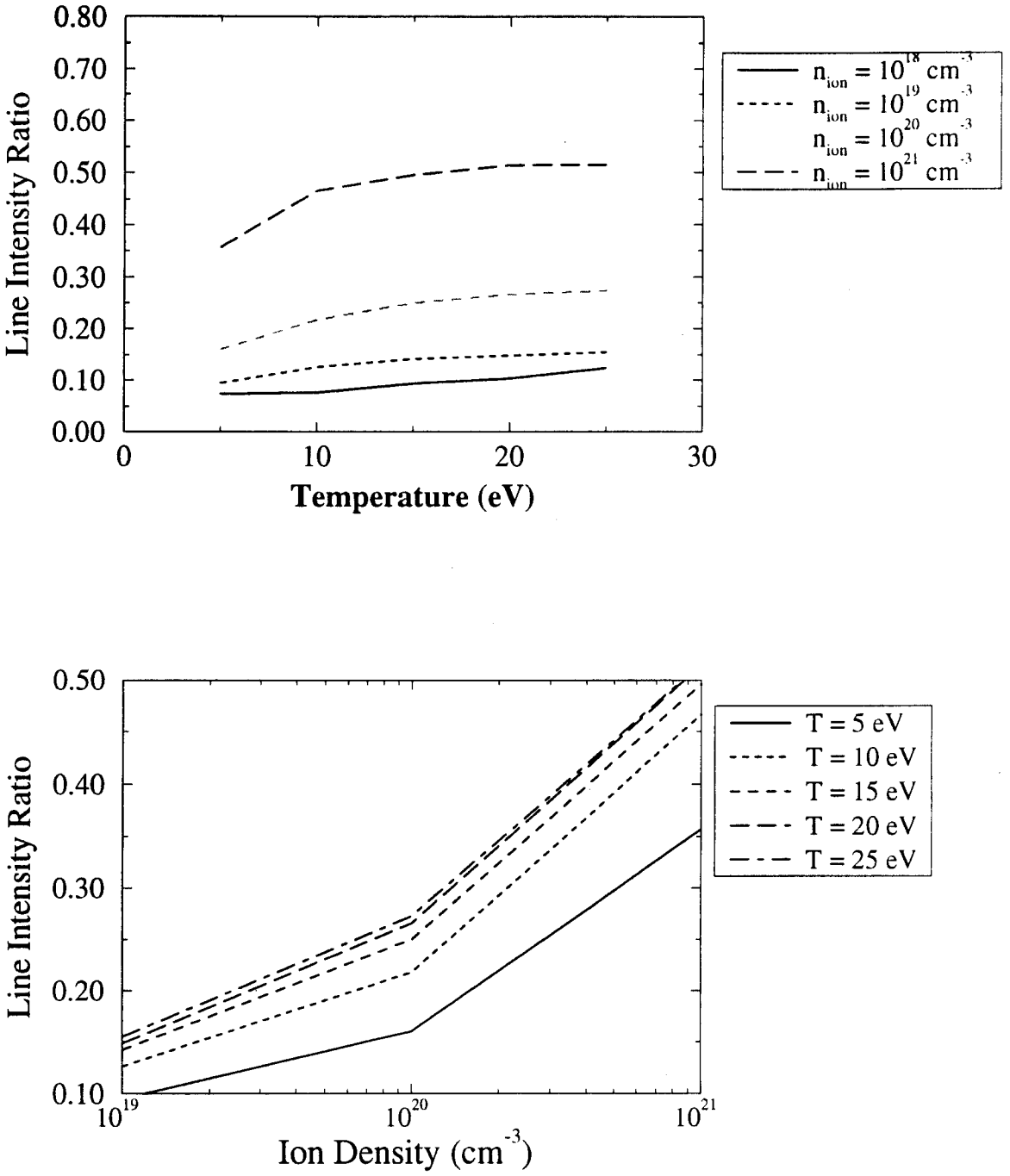

Figure 2.8(f). Temperature and density dependence of Be(λ_5)/Be(λ_4) intensity ratio.

Figures 2.8(d) through 2.8(f) show 3 examples of density-sensitive ratios. In this case, the best density indicators come from lines of the *same* ionization stage. The density dependence arises because the collision excitation rates between autoionizing states begins to exceed proton (beam) impact ionization rates as the dominant mechanism for populating the autoionization states. That is, the population distribution of the autoionizing levels is altered as the electron density increases in this density regime due to collisional excitation and deexcitation between autoionizing levels. Figure 2.8(d) shows the ratio of the Li-like kj and bda lines may be a fairly good density diagnostic. For instance, a measured ratio of 0.2 would indicate a density of $(0.7 - 1.2) \times 10^{21}$ ions/cm^3 over the temperature range of $15 - 25$ eV.

Using measured intensity ratios from K_α lines should prove to be a particularly powerful technique in diagnosing target plasma conditions. Of course, it is important to keep in mind that the plasma changes rapidly with time, and can have significant temperature and/or density gradients. Thus, space- and time-resolved measurements of K_α spectra would be especially valuable.

2.3.5. Summary of K_α Plasma Diagnostics for KALIF Beam Plasma Interaction Experiments

Inner-shell X-ray spectroscopy offers excellent opportunities for diagnosing target plasma conditions in intense light ion beam experiments. We have described how using low-to-moderate-Z tracer materials — such as fluorine, NaF, or MgF — can be used to diagnose plasma conditions in KALIF experiments. Calculations were performed for fluorine to predict the dependence of K_α satellite emission and absorption spectra on temperature and density. Good sensitivity was found for the $2 - 20$ eV temperature range. We have also described how the K_α flux is affected by the tracer and tamper thicknesses. It is recommended that the tracer thickness for KALIF experiments be in the range of $0.1 - 1.0\,\mu$m, with the lower end of this range being used when absorption measurements are to be made.

To analyze K_α spectra measured in KALIF experiments, the following procedures can be used to determine target plasma conditions:

1. Measure K_α emission line intensity ratios with a spectral resolution of $\lambda/\Delta\lambda > 1000$. Perform detailed CRE calculations to independently determine temperatures and

densities using several lines of He-, Li-, and Be-like ions. All intensity ratios should predict approximately the same T and ρ.

2. Perform radiation-hydrodynamics simulations to predict the time- and space-dependence of the target plasma temperature and density. The CRE code can use the predicted $T(r,t)$ and $\rho(r,t)$ to calculate time-dependent and time-integrated spectra which can be compared with experiment.

3. Time-resolved absorption spectral measurements can be made to determine the plasma temperature and density from the relative strengths of individual K_α lines. Again, good spectral resolution is required.

4. Absorption measurements of K_β lines may provide an independent check on the plasma density if sufficiently broadened due to the Stark effect.

If the analysis from each of these techniques is correct, a consistent picture should emerge for the plasma temperature and density, and from that, energy deposition and transport within the target. If the temperature and density can be measured accurately from a single atomic species using these techniques, one could use multiple tracers (or "microdots") at different locations in the target to measure things such as temperature gradients and energy transport. Thus, K_α spectroscopy should provide an extremely valuable diagnostic technique for future KALIF beam-plasma interaction experiments.

3. Determination of Time-Dependent Magnetic Fields by the Observation of Zeeman Splitting of Emission Lines

3.1. Introduction

In pulsed ion-beam diode experiments, magnetic fields may be externally applied or can be produced by the currents flowing in the device. The presence of the magnetic field in the plasma is expected to influence the flow of various ionic species and thus affect the composition of the extracted ion beams. On the other hand, knowledge of the time-dependent diamagnetic effects in the plasma of a pulsed ion-beam diode provides information about the time-dependent current flow in the diode. Hence it is very important to be able to measure time-dependent magnetic fields in the pulsed ion-beam diode.

A common way to measure magnetic fields in pulsed electrically stressed devices is to use magnetic loops. However, in high-power ion-beam diodes the use of magnetic loops is very difficult, and often impossible due to the large currents, the strong electric fields, and the smallness of the diode gap.

Maron et al. [20] have reported on time-dependent measurements of the magnetic field in the plasma of a magnetically insulated ion-beam diode by the observation of Zeeman splitting of spontaneous line emission from heavy ions in the plasma. This method could also be considered for Karlsruhe's ion-beam diode experiments. In the following, we give detailed discussions on the spectroscopic observation of the magnetic field in a high-power-diode plasma by using the Zeeman line spectra. After first outlining the theoretical method for the calculation of the Zeeman spectra, we then compute Zeeman spectra for ions of H, C, Si, and Ba, searching for the 'best candidate' for use in Karlsruhe's ion-beam diode experiments. Finally, we briefly describe the major features of our computational model that can be used for determining magnetic fields from observed Zeeman line spectra. This code is being made available to KfK.

3.2. Zeeman Effect and Zeeman Spectrum

When an atom or ion is subjected to an external magnetic field, the energy levels are split into $2J + 1$ sublevels $M = 0, \pm 1, \pm 2, \cdots, \pm J$, where J is the total angular momentum quantum number. This splitting is the result of the interaction of magnetic field with the ion.

Consider an atom or ion lying in a uniform external magentic field of flux density $\mathbf{B}$. The energy of interaction of the atom with the field is

$$H_{\rm mag} = -\mathbf{B} \cdot \mu, \tag{3.2}$$

where the intrinstic magnetic moment of the atom is given by

$$\mu = -\mu_0[J + (g_s - 1)\mathbf{S}]. \tag{3.3}$$

Here, $g_s = 2.0023192$ is the anomalous gyromagnetic ratio for the electron spin, and $\mu_0 = 4.2543 \times 10^{-10}$ (Ry/gauss) is the Bohr magneton.

To judge whether the magnetic field is *weak* or *strong*, one should compare the energy of the atom in the magnetic field with the spin-orbit interaction $\zeta(LS)\mathbf{L} \cdot \mathbf{S}$. In the *weak-field* case $H_{\rm mag} \ll \zeta(LS)\mathbf{L} \cdot \mathbf{S}$, while in the *strong-field* case $H_{\rm mag} \gg \zeta(LS)\mathbf{L} \cdot \mathbf{S}$. In both the *weak-field* and *strong-field* limits, the energies of Zeeman levels can be calculated with some simple formulae [21]. However, in the general case, energies of the various magnetic sublevels can be found only by diagonalizing the detailed energy matrices with the matrix element of the form:

$$\begin{aligned}
&\frac{1}{\mu_0 B}\langle \alpha LSJM|H(\mathbf{L}\cdot\mathbf{S})\mu_0 B + H_{\rm mag}|\alpha LSJ'M'\rangle \\
&\quad = (M + A)\delta_{JM,J'M'} + (g_s - 1)(-1)^{(L+S+M)} \\
&\quad \times \sqrt{(2J+1)(2J'+1)S(S+1)(2S+1)} \\
&\quad \times \begin{pmatrix} J & 1 & J' \\ -M & 0 & M \end{pmatrix} \begin{Bmatrix} L & S & J \\ 1 & J' & S \end{Bmatrix}.
\end{aligned}$$

Once the eigen-energies and eigenvectors of the magnetic energy matrix are known, the transition strength of the Zeeman lines can be calculated with the following formula:

$$A(\alpha' L' S' J' M' \rightarrow \alpha LSJM) = 2.0261 \times 10^{-6} \cdot \sigma^3 \mathbf{S}\,. \tag{3.4}$$

Here, A is the spontaneous decay rate in the units of s^{-1}, and $\mathbf{S}$ is known as the line strength:

$$\mathbf{S}^{1/2}_{\alpha'\alpha q} = \sum_{\alpha' J'} \sum_{\alpha J} c_{\alpha' J'} c_{\alpha J} \langle \alpha JM|P^{(t)}_q|\alpha' J' M'\rangle \tag{3.5}$$

with

$$\langle \alpha JM|P^{(t)}_q|\alpha' J' M'\rangle = (-1)^{J-M} \begin{pmatrix} J & t & J' \\ -M & q & M' \end{pmatrix} \langle \alpha J\|P^{(t)}\|\alpha' J'\rangle \tag{3.6}$$

where $t = 1$ is for electric dipole transitions. Different q values in above equations correspond to the different polarization of electric dipole radiation. The radiaton with $q = M - M' = 0$ is linear and parallel to the z-axis, while the radiation with $q = M - M' = \pm 1$ is elliptically polarized and perpendicular to the z-axis. The former is called π radiation and the latter σ radiation. It should be noted that experimentally the σ radiation can only be collected parallel to the magnetic field, while the π radiation is collected perpendicular to the magnetic field.

3.3. Zeeman Spectrum Analysis

In order to be able to determine the magnetic field strength from the spectral line profile, the Zeeman splitting must dominate over other contributions to the line profile. The main broadening mechanisms we consider here are Zeeman splitting and Doppler broadening. We do not consider instrumental broadening in the calculations discussed below. (This effect is included in our model, but because this parameter is not known we have chosen not to consider it at the present time.) A spectral resolution of 0.1 Å is required for magnetic fields $\approx 4 - 8$ kG [20]. If the Zeeman splitting is small compared to the other broadening mechanisms, the dependence of spectral line profile on magnetic field strength will be very insignificant. The use of longer wavelength lines is preferable because of the relative increase of the Zeeman splitting (over the Doppler broadening) with the wavelength. The Zeeman spectrum of several lines with wavelength of ~ 6000 Å will be studied here. The purpose of the study is to identify lines which may be good candidates for measuring B-field strengths.

The Zeeman splitting of the hydrogen $3d_{5/2} \rightarrow 2p_{3/2}$ transition for 3 different magnetic field strengths is shown in Figs. 3.1 and 3.2. Only σ components are shown here. Also shown in the figures are the corresponding spectra with a Gaussian spectral profile which includes the effects of Doppler broadening for each component. It is seen from the figures that for a magnetic field of $B > 5$ kG the spectral shift of each component relative to the line center is $\gtrsim 0.1$ Å. However, since hydrogen is a very light element, the Doppler broadening completely dominates over the Zeeman splitting under the experimental conditions of interest for KALIF ($B \sim 1-10$ kG, $T_p \sim 5-20$ eV). Because of this, it is very hard to obtain magnetic field information from Zeeman spectral line profiles of hydrogen.

Figure 3.3 shows the Zeeman spectra of the C II $1s^2 2s^2 3p^1\ ^2P_{3/2} \rightarrow 1s^2 2s^2 3s^1\ ^2S_{1/2}$ transition at 8 kG magnetic field and three different ion temperatures. As shown in the

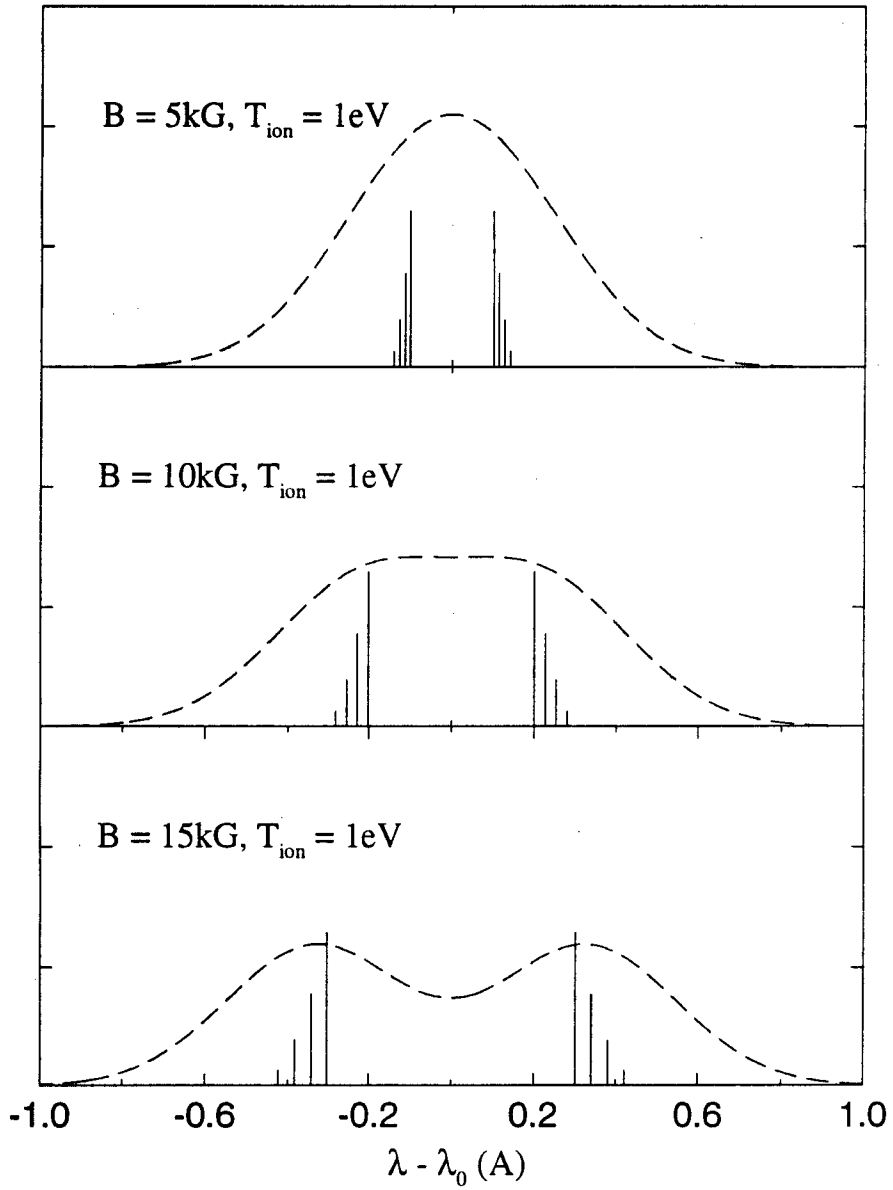

Figure 3.1. Computed Zeeman pattern of the H I $3d_{5/2} - 2p_{3/2}$ transition at $T_{\rm ion} = 1$ eV and various magnetic fields . Both schematic form and line profile are shown.

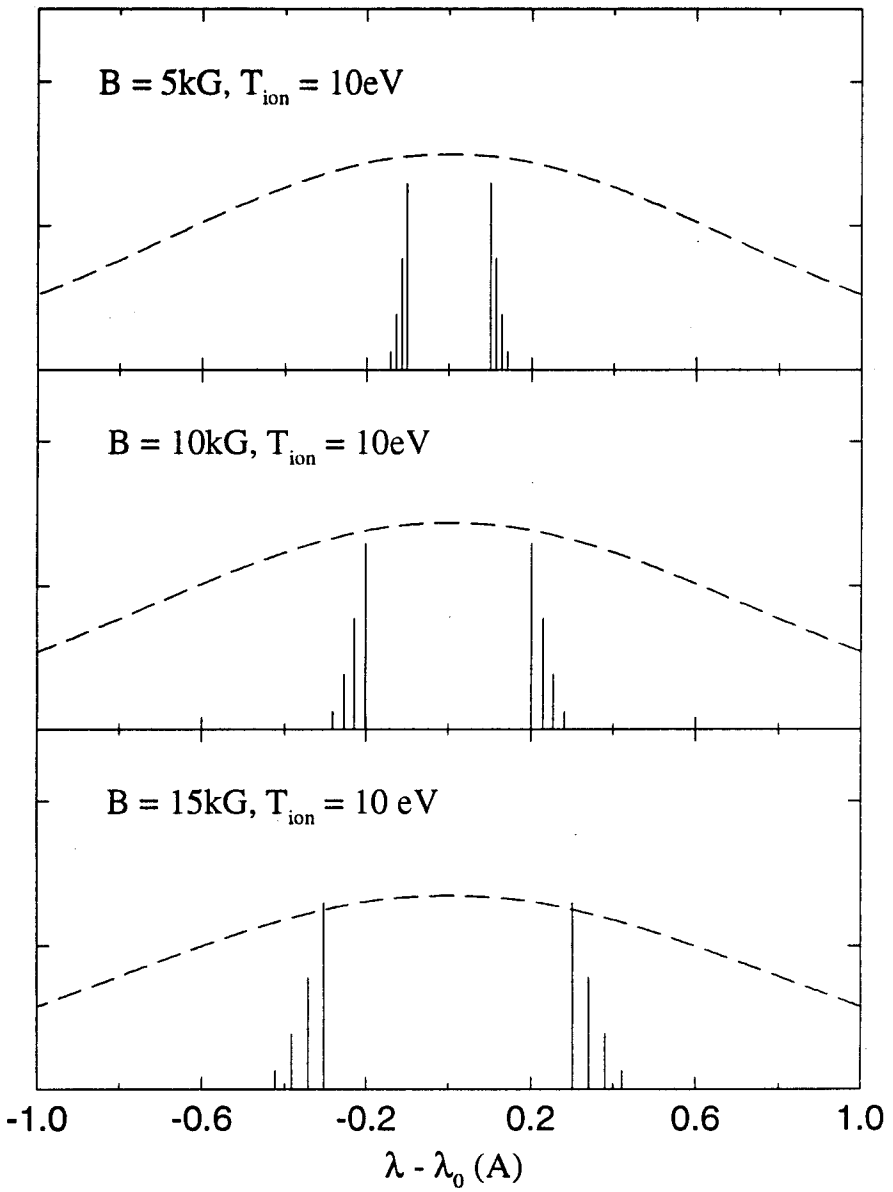

Figure 3.2. Computed Zeeman pattern of the H I $3d_{5/2} - 2p_{3/2}$ transition at $T_{\rm ion} = 10$ eV and various magnetic fields. Both schematic form and line profile are shown.

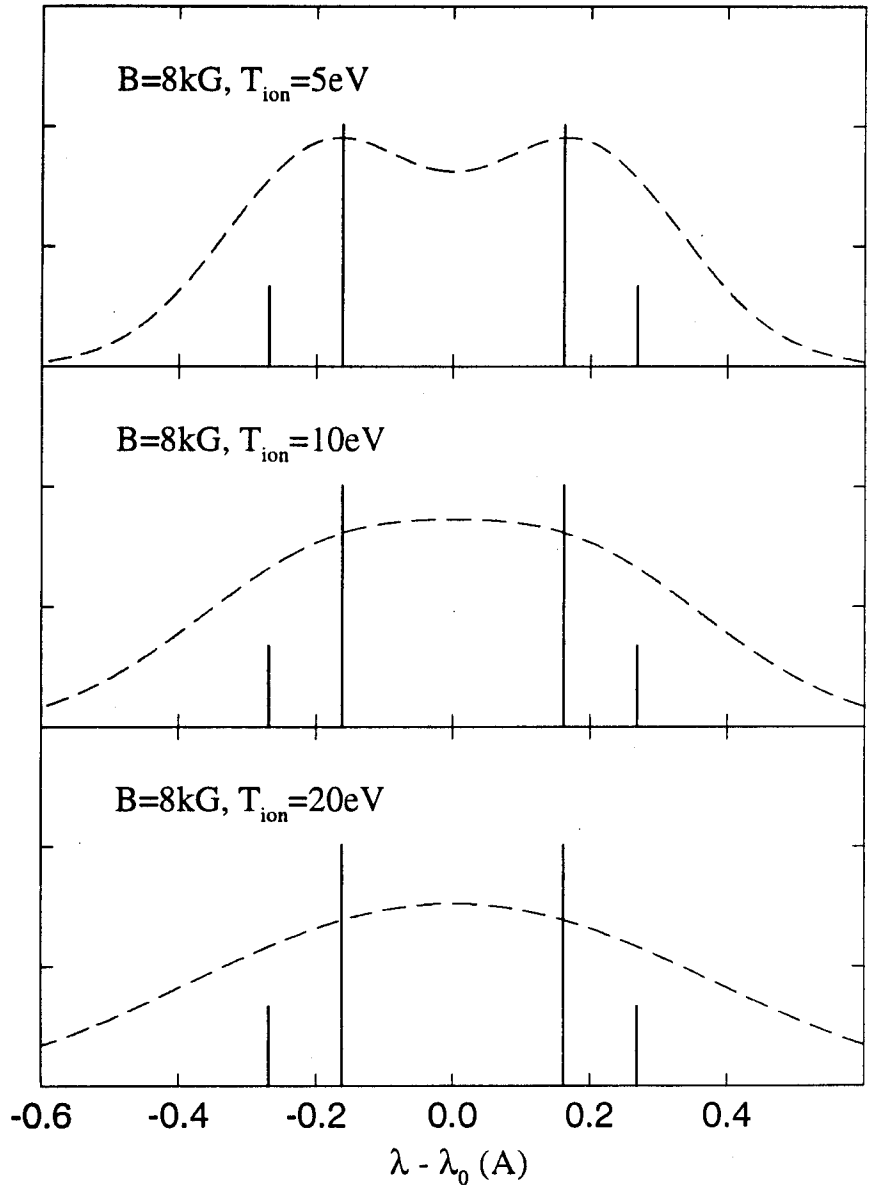

Figure 3.3. Computed Zeeman pattern of the C II $3p^1\,^2P_{3/2} - 3s^1\,^2S_{1/2}$ transition at 8 kG and three different ion temperatures. Both schematic form and line profile are shown.

figure, the Zeeman splitting characteristics can only be seen at relatively low temperatures ($T_{\rm ion} \lesssim 5$ eV) because the Doppler broadening becomes small. At higher temperatures, which should be closer to the experimental values, the Zeeman splitting is hidden by the Doppler broadening.

A comparison of Zeeman splitting and Doppler broadening for C II at various magnetic field strengths and ion temperatures is shown in Fig. 3.4. Also shown is the effect of Doppler broadening on Zeeman spectrum. It is seen that in order to clearly observe the Zeeman splitting characteristics in a spectral line profile, the Zeeman splitting should be at least 1.5 to 2 times larger than the Doppler broadening. The Zeeman splitting of C II lines is likely to be too small compared to the Doppler broadening to be used for measuring magnetic fields for the experimental conditions of KALIF.

Figure 3.5 shows a comparison of Zeeman splitting and Doppler broadening with $T_{\rm ion} = 5$ eV at various magnetic field strengths for the Si II $3s^2 4p^1\,{}^2P_{3/2} \rightarrow 3s^2 4s^1\,{}^2S_{1/2}$ transition. The dependence of the relative broadening due to the Zeeman and Doppler effects of this Si II line on B field and ion temperature is shown in Fig. 3.6. It is seen that the Zeeman splitting does not significantly exceed the Doppler broadening until $B \approx 5 - 8$ kG when $T_{\rm ion} = 5$ eV, and $B \approx 10 - 13$ kG kwhen $T_{\rm ion} = 20$ eV in the shown conditions of B field and ion temperature. Hence, this line does not appear to be a particularly good candidate for measuring B field strengths.

Since the ion velocities in the plasma are found to be smaller for heavier ions, the Doppler broadening effect can be reduced by using emission lines of heavy ions. It has been suggested [20] that the Zeeman spectra of the Ba II $5p^6 6p^1\,{}^2P_{3/2} \rightarrow 5p^6 5d^1\,{}^2D_{5/2}$ transition (the 6142 Å line) is a very good candidate for B-field measurements for conditions of $B \sim 4 - 10$ kG and $T_{\rm ion} \sim 20$ eV. The calculated spectral profiles of the Ba II 6142-Å line with $T_{\rm ion} = 15$ eV and different magnetic fields are shown in Fig. 3.7. A comparison of Zeeman splitting and Doppler broadening at various magnetic field strengths and plasma temperatures is shown in Figure 3.8. It can be seen that the Zeeman splitting pattern is clearly observed in all cases, and the line profile is very sensitive to the magnetic field. In Maron's experiment [20], Ba II ions were added to the anode plasma by mixing the epoxy used for the anode with 60% by weight of BaF_2 powder.

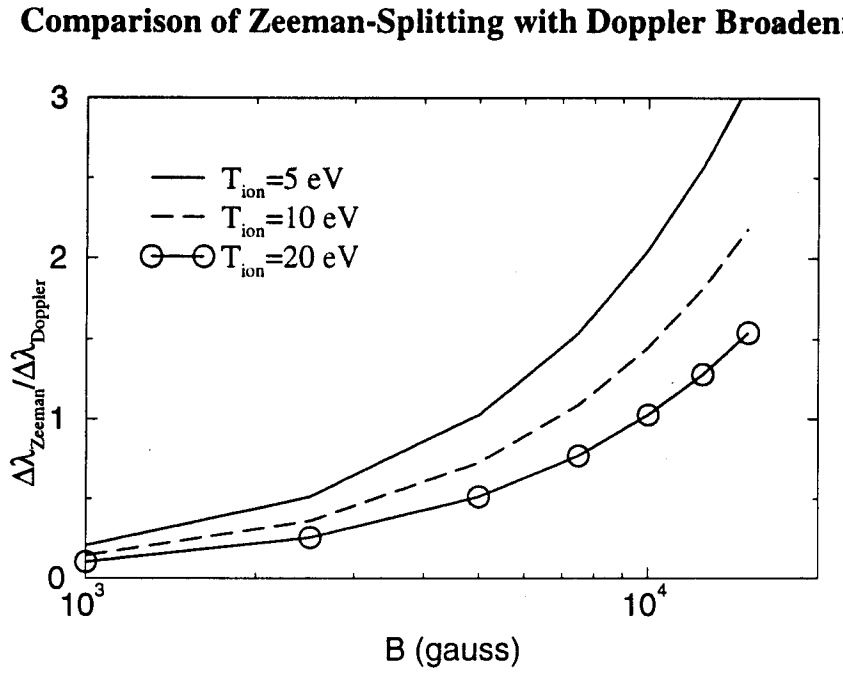

Figure 3.4. (a) B-T curves: Comparison of Zeeman splitting with Doppler broadening at different magnetic field and ion temperature conditions for C II $3p^1\,^2P_{3/2} - 3s^1\,^2S_{1/2}$ transition. (b) Effect of Doppler broadening on Zeeman line profile.

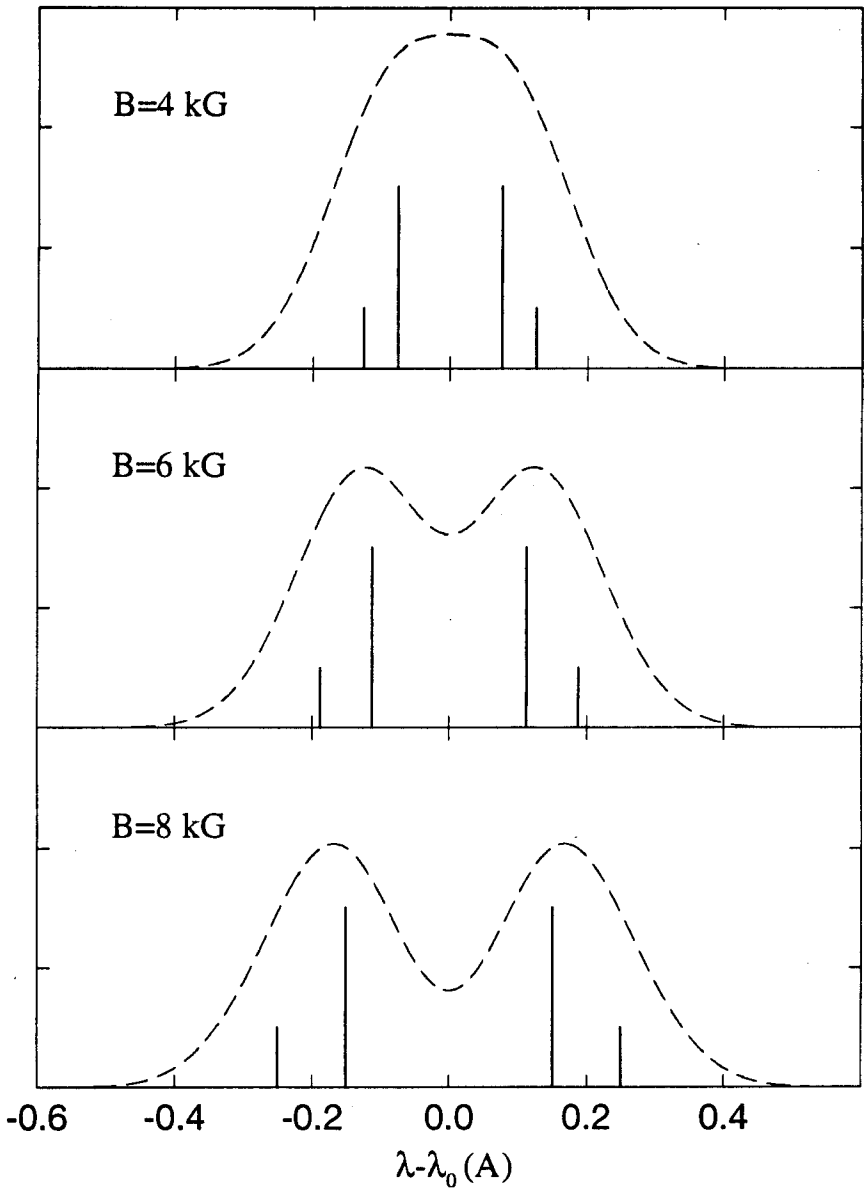

Figure 3.5. B-T curves: Comparison of Zeeman splitting with Doppler broadening at different magnetic field and ion temperature conditions for Si II $4p^1\,^2P_{3/2} - 4s^1\,^2S_{1/2}$ transition.

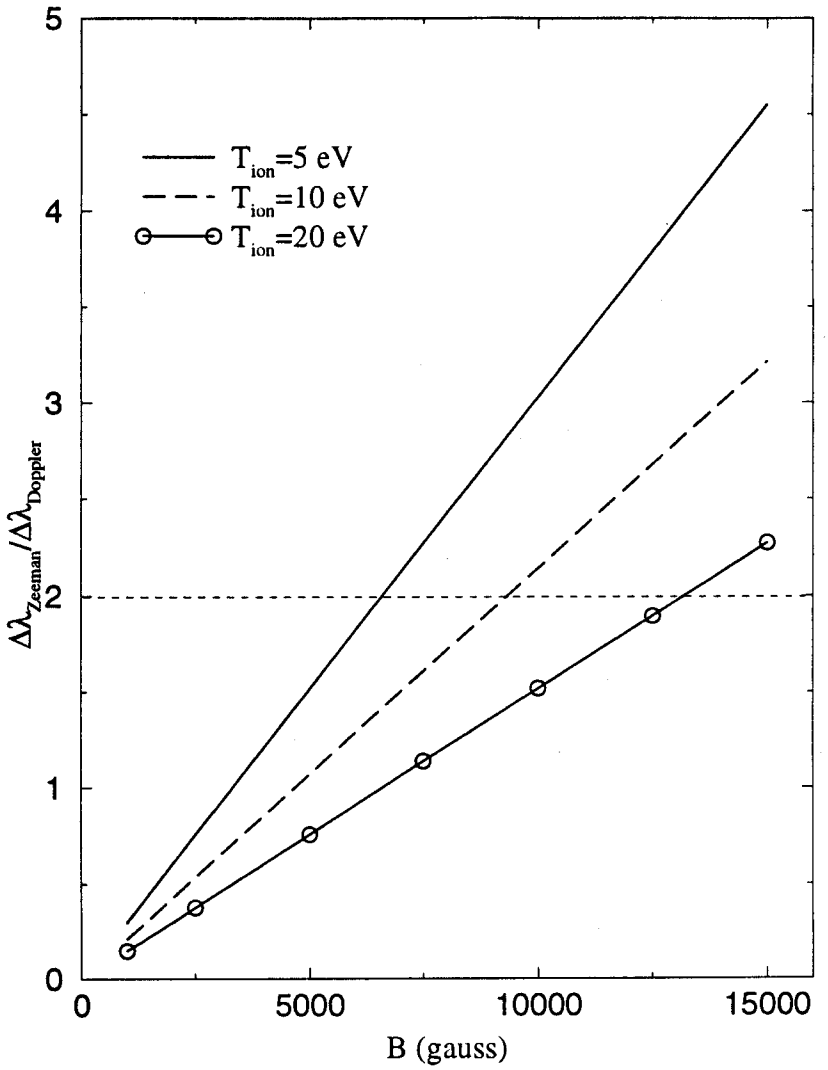

Figure 3.6. Computed Zeeman pattern of the Si II $4p^1\,^2P_{3/2} - 4s^1\,^2S_{1/2}$ transition at $T_{\rm ion} = 5$ eV and various magnetic fields. Both schematic form and line profile are shown.

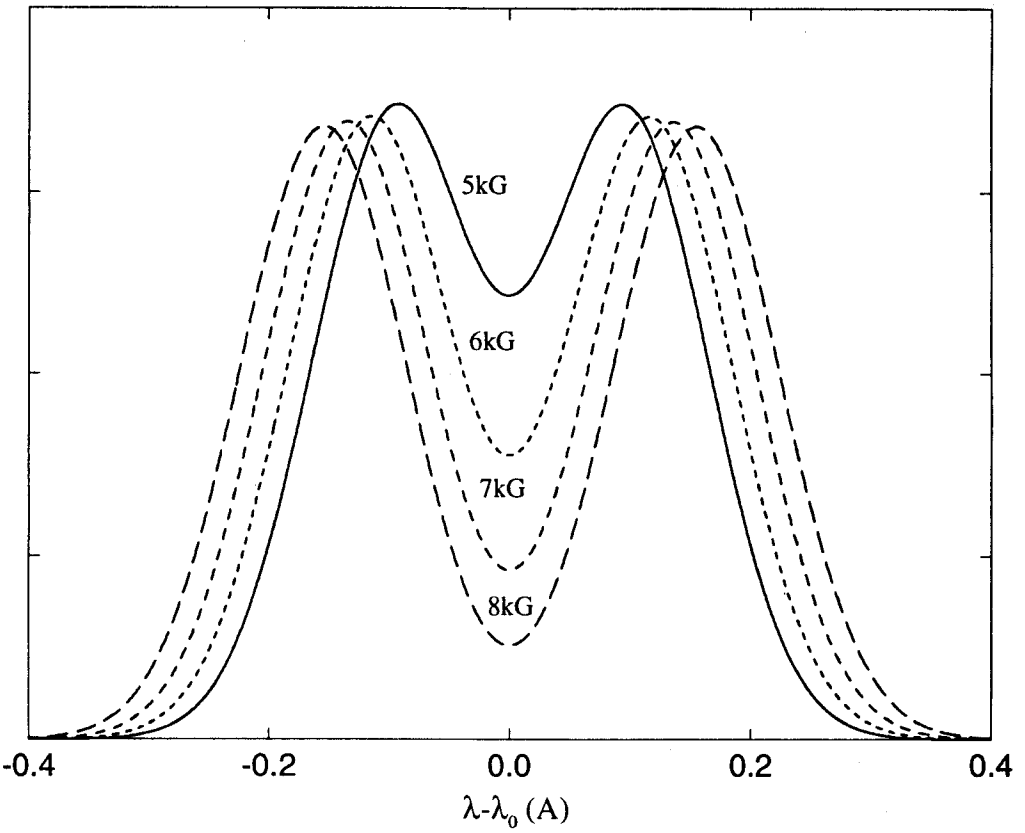

Figure 3.7. Sensitivity of Zeeman line profile to magnetic fields for Ba II 6142 Å line.

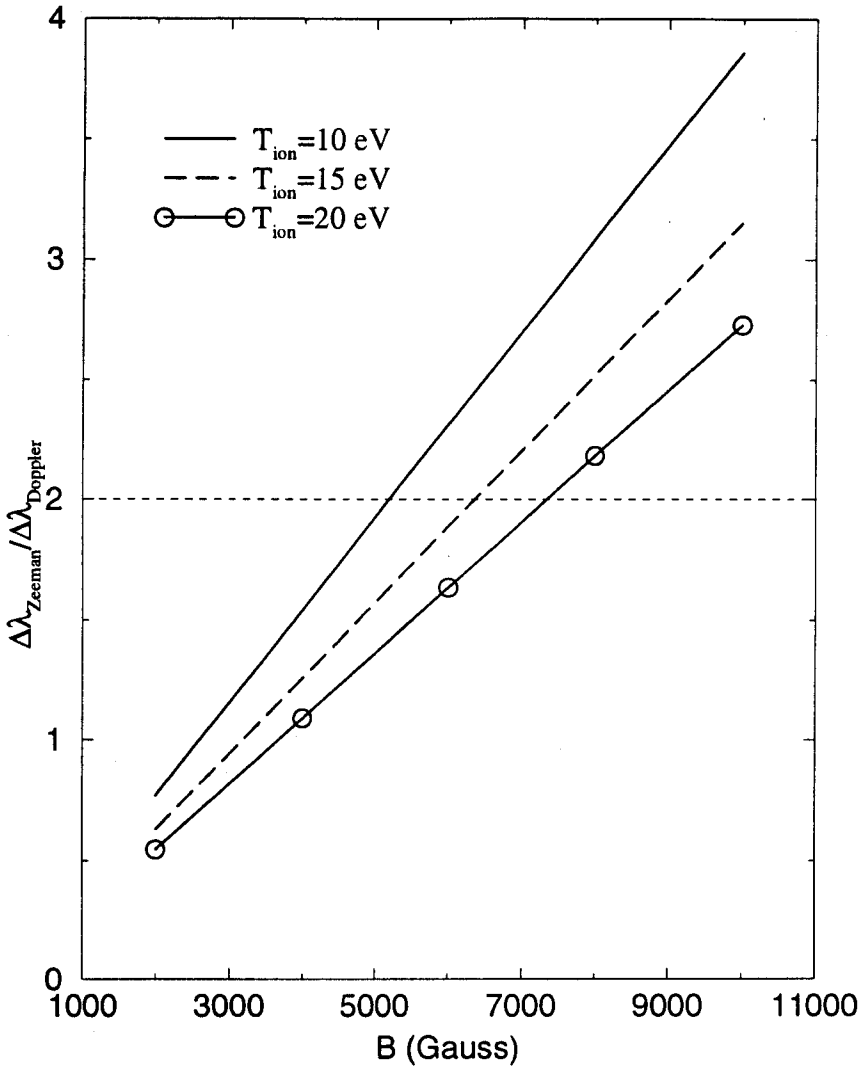

Figure 3.8. B-T curves: Comparison of Zeeman splitting with Doppler broadening at different magnetic field and ion temperature conditions for the Ba II 6142 Å line.

3.4. Computer Code for Zeeman Spectrum Analysis

The basic idea of using the Zeeman spectrum to measure the magnetic field in high power diode plasmas is that the magnetic field can be determined by best fitting the observed spectral line profile if the Zeeman splitting dominates over other contributions to the line profile. In order to obtain a reliable determination of the magnetic field strength from the observed data, it is necessary to calculate the Zeeman splitting emission pattern accurately. This includes the energies of Zeeman splitting levels and component intensities of Zeeman splitting lines.

We have developed a computer code, B-FIT, which can do detailed Zeeman spectrum analysis. In this code, the detailed energy matrix of both magnetic field interaction and spin-orbit interaction is computed and diagonalized to determine the Zeeman energy levels. The important level interaction effects can also be included if necessary. Hence the Zeeman-split emission pattern of a specified line can be calculated accurately for a wide range of magnetic fields ($0 < B < \infty$), as opposed to models which are accurate in only the high B-field limit or low B-field limit. Some benchmark results are shown in Fig. 3.9, where an experimental spectrum and two computed Zeeman patterns are shown. Figure 3.9(a) shows the computed Zeeman patterns with weak-field Zeeman splitting formulas. Fig. 3.9(b) is the schematic form of the computed Zeeman patterns from our computer code B-FIT. Fig. 3.9(c) compares an experimental spectrum (solid curves) of the Ge II $3d^{10}4d^{1\,2}D_{5/2} - 3d^{10}4f^{1\,2}F_{5/2,7/2}$ transitions at 24 kG with Cowan's computed Zeeman pattern (dashed and solid vertical lines) [21]. It can be seen that the result from B-FIT agrees very well with the experimental data, while the splittings calculated with the weak-field model are less accurate.

This code is being made available to KfK.

3.5. Summary and Suggestions

Magnetic fields in the anode plasmas of ion-beam diodes can be measured by the observation of Zeeman splitting of line emission from heavy ions. The advantage of using the lines of heavy ions lies not only in the small Doppler broadening of these lines, but also in the fact that the heavy ions remain close to the anode surface throughout the entire pulse. This allows one to measure the magnetic field very close to the anode surface with a high spatial resolution. Magnetic field strengths can be determined from emission lines when the Zeeman splitting is large compared to other broadening mechanisms.

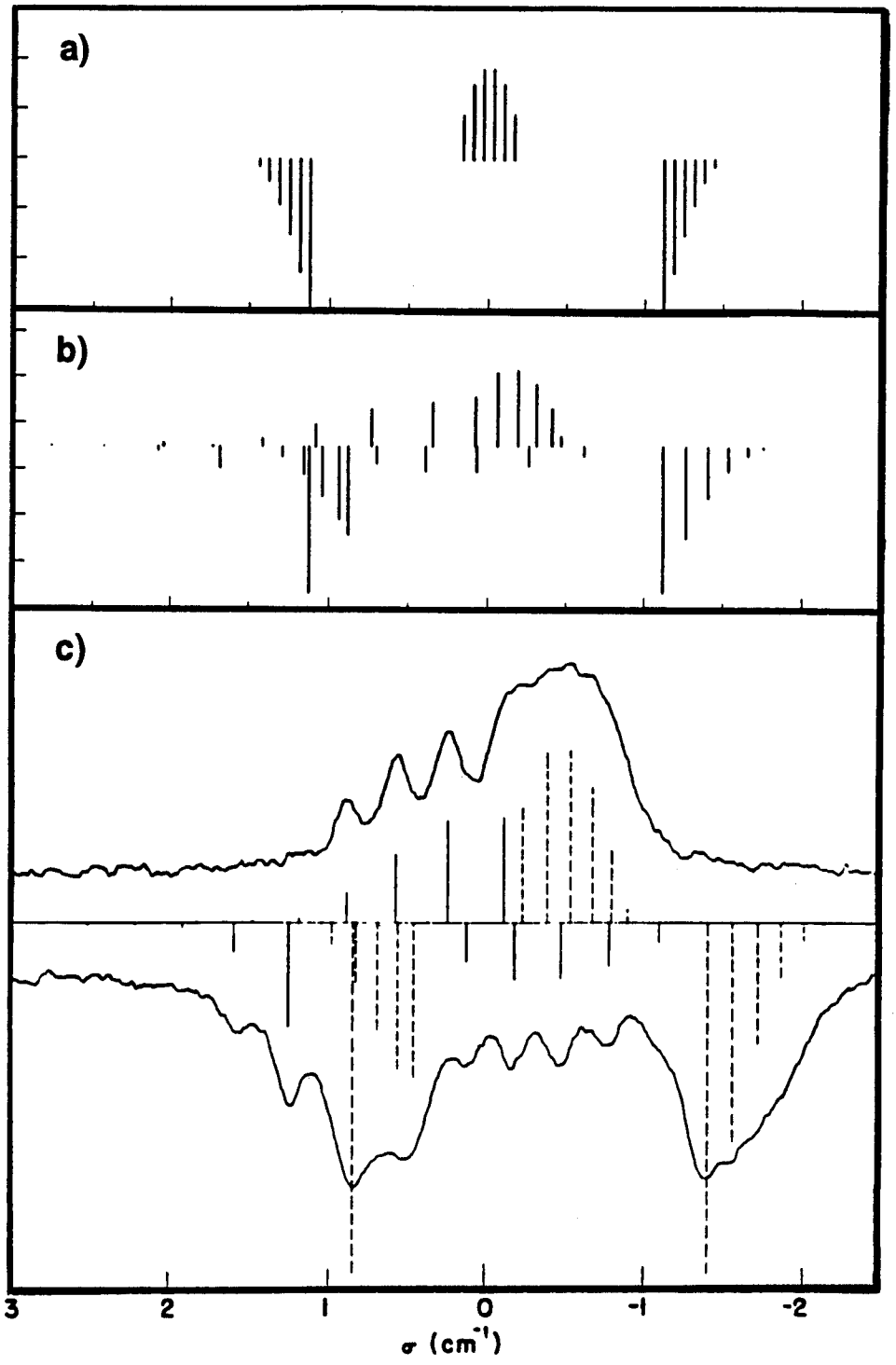

Figure 3.9. Zeeman spectrum of the Ge II $4d\,^2D_{5/2} - 4f\,^2F_{5/2,7/2}$ transition at 24 kG: (a) computed Zeeman pattern with "weak" field model; (b) our calculation (B-FIT); (c) experimental data and Cowan's calculated results.

The Zeeman splitting should be at least 1.5 times larger than the other broadening effects. In order to observe Zeeman splitting of a fraction of an angstrom, a spectral resolution of 0.1 Å is required. This may be obtained by using optical magnification at the spectrograph output and a fiber-photomultiplier tube system [22]. Time-dependent data of the spectral line profile taken by the high resolution system can be analyzed with our B-FIT computer code. B-FIT can determine the time-dependent magnetic field from a best fit of the computed emission pattern to the experimental data points.

4. Users' Guides for Non-LTE Radiative Transfer and Atomic Physics Codes

We have completed users' guides for our non-LTE (LTE ≡ local thermodynamic equilibrium) radiative transfer and atomic physics codes which have been installed on the KfK computing facilities. The three users' guides are as follows:

(1) NLTERT – A Code for Computing the Radiative Properties of Non-LTE Plasmas.

This is a collisional-radiative equilibrium (CRE) code which can be used for spectral diagnostics analysis studies of ion beam-heated plasmas.

(2) ATBASE User's Guide.

This is a suite of atomic physics codes which computes atomic structure data, oscillator strengths, collision cross sections, and various rate coefficients for plasmas. It supplies the atomic data bases for NLTERT (Item 1) and the CRE algorithms of KATACO (Item 3).

(3) CRE Model for the KATACO Radiation-Hydrodynamics Code.

The CRE algorithms incorporated into KATACO provide the capability to more accurately simulate non-LTE line radiation transport effects in high energy density plasmas.

In some versions of this report, the users' guides are included in the remainder of Section 4. In other versions, the users' guides are supplied separately in 3-ring binders to both provide a more convenient format for those utilizing the codes, as well as to allow for updating the documentation quickly and easily.

Acknowledgements

The authors gratefully acknowledge the support of Kernforschungszentrum Karlsruhe through Fusion Power Associates.

References

1. A. Hauer, R. D. Cowan, B. Yaakobi, O. Barnouin, and R. Epstein, Phys. Rev. **A 34**, 411 (1986).

2. C. Chenais-Popovics, C. Fievet, J. P. Geindre, J. C. Gauthier, E. Luc-Koenig, J. F. Wyart, H. Pepin, and M. Chaker, Phys. Rev. **A 40**, 3194 (1989).

3. J. Bruneau, C. Chenais-Popovics, D. Desenne, J.-C. Gauthier, J.-P. Geindre, M. Klapisch, J.-P. Le Breton, M. Louis-Jacquet, D. Naccache, and J.-P. Perrine, Phys. Rev. Lett. **65**, 1435 (1990).

4. T. S. Perry, S. J. Davidson, F. J. D. Serduke, D. R. Bach, C. C. Smith, J. M. Foster, R. J. Doyas, R. A. Ward, C. A. Iglesias, F. J. Rogers, J. Abdallah, Jr., R. E. Stewart, J. D. Kilkenny, and R. W. Lee, Phys. Rev. Lett. **67**, 3784, (1991).

5. P. T. Springer, T. S. Perry, D. F. Fields, W. H. Goldstein, B. G. Wilson, and R. E. Stewart, *Atomic Processes in Plasmas*, AIP Conference Proceedings 257, E. S. Marmer and J. L. Terry, eds., Amer. Inst. Phys., New York (1992).

6. J. M. Foster, D. J. Hoarty, C. C. Smith, P. A. Rosen, S. J. Davidson, S. J. Rose, T. S. Perry, and F. J. D. Serduke, Phys. Rev. Lett. **67**, 3255 (1991).

7. P. Beiersdorfer, T. Phillips, V. L. Jacobs, K. W. Hill, M. Bitter, S. von Goeler, and S. M. Kahn, Astrophys. J. **409**, 846 (1993).

8. A. R. Knudson, D. J. Nagel, P. G. Burkhalter, and K. L. Dunning, Phys. Rev. Lett. **26**, 1149 (1971) .

9. R. L. Watson, O. Benka, K. Parthasaradhi, R. J. Maurer, and J. M. Sanders, J. Phys. **B 16**, 835 (1983).

10. J. Bailey, A. L. Carlson, G. Chandler, M. S. Derzon, R. J. Dukart, B. A. Hammel, D. J. Johnson, T. R. Lockner, J. Maenchen, E. J. McGuire, T. A. Mehlhorn, W. E. Nelson, L. E. Ruggles, W. A. Stygar, and D. F. Wenger, Lasers and Particle Beams **8**, 555 (1990).

11. J. J. MacFarlane, P. Wang, J. Bailey, T. A. Mehlhorn, R. J. Dukart, and R. F. Mancini, Phys. Rev. E **47**, 2748 (1993).

12. J. E. Bailey et al., Proceedings of the 6th International Workshop on Atomic Physics for Ion Driven Fusion, Santa Fe, NM (1993).

13. J. J. MacFarlane, P. Wang, J. E. Bailey, T. A. Mehlhorn, and R. J. Dukart, Proceedings of the 6th International Workshop on Atomic Physics for Ion Driven Fusion, Santa Fe, NM (1993).

14. B. Goel, Proceedings of the 6th International Workshop on Atomic Physics for Ion Driven Fusion, Santa Fe, NM (1993).

15. J. E. Bailey, private communiction (1993).

16. J. P. Apruzese, J. Davis, D. Duston, and K. G. Whitney, J.Q.S.R.T. **23**, 479 (1980).

17. J. J. MacFarlane, P. Wang, et al., Fusion Power Associates Reports FPA-90-1 (1990), FPA-91-1 (1991), and FPA-92-1 (1992).

18. W. Brandt and G. Lapicki, Phys. Rev. **A 23**, 1717 (1981).

19. J. J. MacFarlane and P. Wang, Fusion Power Associates Reports FPA-93-3 (1993).

20. Y. Maron E. Sarid, E. Nahshoni, and O. Zahavi, Phys. Rev. **A39**, 5856 (1989).

21. R. D. Cowan, *The Theory of Atomic Structure and Spectra*, University of California Press, 1981.

22. Y. Maron, E. Sarid, O. Zahavi, L. Perelmutter, and M. Sarfaty, Phys. Rev. **A39**, 5842 (1989).

Appendix A

Plasma Diagnostics Using K_α Satellite Emission Spectroscopy in Light Ion Beam Fusion Experiments

J.J. MacFarlane and P. Wang

(Submitted for publication to *Lasers and Particle Beams* as part of the 6th International Workshop on Atomic Physics for Ion Driven Fusion.)

Appendix B

Effects of Multiple Ionization on the K_α Spectrum of Aluminum in Intense Lithium Beam Experiments

P. Wang, J.J. MacFarlane, G.A. Moses

(Submitted for publication to *Lasers and Particle Beams* as part of the 6th International Workshop on Atomic Physics for Ion Driven Fusion.)